Measurement of 3D deformation in transient phenomena

Doctorate of Science (Optics)

Student: M. C. Carlos Mares Castro

Adviser: Dr. Bernardino Barrientos García

December 2017
León, Guanajuato, México

To

God, our Father, who gives us the opportunity to admire the wonders of nature and gives us the instruments to develop the science.

Chela, my wife, for her support and understanding.
Carlitos, my beloved son, who is my big motivation in life.

José Luis and M. Luisa, my parents, who are my greatest examples of perseverance and unconditional support.

Myriam, José Luis, Rubén, Rafael (who rest in peace), Magdalena, Efraín, Estela, Alfredo and Armando, my brothers and sisters, who have always accompanied me in my life.

Myriam, Jacqueline, Marlene, Naomi, Rafita, Arely, Wendy, Valeria, Josué, Paquito, Andrea, Irazú, and Mariane, my nieces and nephews, who are a source of joy and motivation.

All other members of my family, cousins, aunts, uncles, grandparents, etc.

Classmates of Instituto Tecnológico de León.

Dedicated to all of them

Acknowledgements

I am thankful to CONACyT, for having granted me a doctorate scholarship.

I would like to express my deepest gratitude to CIO and my teachers and personnel who were related with the development of this work. Likewise, my thanks to my colleague students for their friendship and assistance in some academic activities.

Also, I am indebted to Dr. Bernardino Barrientos García for his continuous guidance on the topic discussed in this work. Additionally, to M. C. Ricardo Valdivia Hernández, who assisted me on the implementation of some illumination systems. Further, I am indebted to Dr. Mariano Cerca Martínez and Dr. Damiano Sarocchi for their collaboration on the implementation of the geological models.

I want to express my thanks to the guidance committee, Dr. Amalia Martínez García and Dr. Carlos Pérez López, for their attention throughout the doctorate period.

Besides, my sincere acknowledgments to the reviewers of this work, for their useful comments and suggestions: Dr. Mariano Cerca Martínez and Dr. Carlos Pérez López.

Measurement of three-dimensional displacement in transient events

Contents

Summary

Three-dimensional deformation of objects is an important topic when evaluation of performance of mechanical systems is of interest. Deformation can be measured by classical methods, by using strain gauges, for example. However, in these types of methods, it is necessary that the sensor is in contact with the object, and generally they are point-wise. Optical methods can deal with those limitations, and even add further abilities such as automatization. Among optical methods, fringe projection (FP) and digital image correlation (DIC) have shown potentiality to be used in industrial environments. However, FP can only yield the out-of-plane component of displacement and DIC the two in-plane components of displacement. As shown in previous works, combination of both techniques, called here FP-DIC, allows us to obtain the three components of displacement, but separated in time.

In this work, we present a variation of FP-DIC that enables us to use FP and DIC simultaneously. As a consequence, dynamic events can be fully analyzed. In addition to show simultaneity, the technique has been extended as to cover objects that are not neutral in color, as generally assumed, but multi-colored, which is a more realistic situation in industry. The optimization of the light source for multi-colored objects is examined by means of a contrast analysis. Additionally, the objects under analysis may even present relatively high dynamic range of intensity levels. This latter feature is dealt with by incorporating an independent light source for DIC (an additional advantage is the analysis of surfaces that may contain a large range of values of roughness).

Feasibility of the technique is shown through two application examples: the analysis of an avalanche and the compression of a layered model, both in the field of geology.

1 Background and motivation

Designing and optimization of mechanical devices involves characterization and modeling of the parts, from distinct points of view, for example those concerning dynamics and electromagnetics. The related analysis is commonly carried out by analyzing the influence of physical parameters on the performance of the device. If the device will be used under mechanical load, one of those parameters is mechanical displacement, which is defined as the change in position of any point of a system, when an external disturbance is applied. In general, the displacement can be represented by a space vector, which is composed by three components. When the object displacement is to be assessed by an optical method, it is common the use of a camera (combination of a sensor and an imaging lens). In this case, an arbitrary displacement may be decomposed into the following components: an out-of-plane component (OOP) that is in the direction of the optical axis of the imaging lens, and two other components, the in-plane components (IP), which are perpendicular to the optical axis and that are perpendicular to each other.

Displacement in objects may be regarded as the difference of object shape between two different states that are separated in time. Considering this definition, then any technique capable of measuring shape can be used to measure displacement.

There are several optical methods that are able to assess shape, among them we can mention interferometric methods [1-3] and white-light methods [4, 5]. The first types are characterized by their extremely high sensitivity and resolution, on the order of a few micrometers, and accordingly, to produce reliable results, they need a relatively stable ambient, such as that found in labs. On the other hand, white-light methods, like moiré and digital image correlation, present sensitivities that may be readily under control of a user and they are practically immune to external disturbances, making them good candidates to be used in industrial environments. In this thesis work a major aim is to measure displacement under industrial environments, and under transient conditions. To accomplish with the latter feature, we resort to optical methods that do not require the use of multiple images, such as fringe projection (FP) [6-14] and digital image correlation (DIC) [15-21].

In both FP and DIC, the object under test is illuminated by a spatially/uniform light beam; the light source may correspond to any incoherent light source, such as a lamp or an LED. In FP, the spatial structure corresponds to a fringe pattern, and in

DIC, to a pattern with randomly-located spots (a uniform beam of light can also serve this purpose). In the two techniques, two images of the object are registered by a camera, one before displacement and another after displacement. The images are then compared and the desire information is obtained: out-of-plane deformation by FP, and in-plane displacement by DIC. It is important to point out the use of only one image per state. As FP can yield only the OOP and DIC the IP, one technique at a time is not enough to render the three-dimensional state of the object. However, when combined, they naturally complement each other, as their range of displacement is fairly the same.

Some works have made use of each technique, FP and DIC, separately [22-24]. Evidently, the study of dynamic events cannot be done. This restriction arises from the fact that the illumination type of each technique is different and has to be changed during one measurement. This limitation can be overcome, by for example spectrally separating the information for the two techniques and using color filters [25]; the drawback is that two light sources and two cameras have to be used. As described in the present thesis work, by encoding the spatial signals of the two techniques in the RGB channels of color images, it is possible the use of only one camera and one light source, and no color filters at all. Another approach to enable the analysis of dynamic events was proposed by [26]; only one image is used; the projected image contains a fringe pattern, and the necessary texture (white-speckle) image is obtained from the recorded fringe pattern via Fourier transform: the recorded image is transformed and a low-pass filter is applied; then, the result is inverse transformed and an image free of fringes is generated (this image is used for correlation purposes). The main drawback of this technique is that in order to get fringe-free images, the average size of the speckle structure of the object should be larger than the fringe period (in this way, the spectral content of the speckle field does not overlap the first spectral side-lobe of the fringe pattern). This may limit the size of the region of interest and the range of in-plane displacements.

One third approach [27] reports an alternative for dynamic measurements. In this case, the signals for both DIC and FP are encoded in the RGB signal of a color image. Color encoding has been used in 3D shape recovering [28, 29], fluid studies [30, 31], and phase stepping [32-36]. As shown in Ref. 27, the necessary information for measuring 3D displacement is contained in just one RGB image, and calibration procedures are not required as in methods that use multiple cameras, such as 3D DIC [37, 38]. In Reference 27, red spots (speckles) that

serve as the DIC signal are directly printed onto the object surface and fringes with blue and white portions are projected simultaneously. By the use of a color camera, the signals for DIC and FP can then be separated. However, as the red spots appear in the fringe information they reduce the accuracy of the technique; to alleviate the problem, application of a directional filter was applied. In [39], we propose an improvement to the color encoding technique that reduces significantly the presence of speckles in the image of fringes, thus increasing the accuracy of the technique.

In our case [39, 40], the FP and DIC illumination patterns are encoded on the blue and red channels of a digital projector. Then, as the illumination beam impinges on the object —a white object with a diffusive surface is generally assumed—, the light is modulated by the reflectance of the surface and then reflected onto a digital color camera. The camera yields images composed of three gray-level images, each corresponding to the three primary colors, RGB, which in turn are related with the color filters of the sensor. One of these gray-level images carries the FP information and another, the DIC information. After the registering of the images, they are separated by software and from then onwards, they can be used for analysis. The first part of the work deals with the analysis of this technique variation (named here FP-DIC); some parameters of the combined setup, such as period and subimage size, are subjected to evaluation in order to optimize the technique. Besides, a numerical simulation of the influence of the residual speckle in the FP image is presented. The principal aim of this part is to show the feasibility of the technique. To accomplish with this purpose we measure known three-dimensional arbitrary displacements given to a metallic plate, and the accuracy is calculated. The plate is placed on a mechanical stage driven by step motors, which produce displacements in three mutually perpendicular directions. These types of measurements are static, but transient events can be equally well analyzed, which is the main objective of the work, as further described in Chapter 5.

When the technique was used in a real application, for example the measurement of displacement of the free surface of an avalanche, where real raw materials are used (sands taken directly from volcanoes), we realized that the obtained results lacked of accuracy because of the high content of noise in the images. The noise level mainly arose from the low contrast of the color content of the sands. This limitation obliged us to evaluate the performance of the technique when applied to either neutral-colored objects or multicolored objects. The analysis concerning this latter

point is included in the second part of the work, Chapter 4. First of all, a model of neutral-colored surface is presented. Later, this model is extended to cover a multi-colored object. Characteristic parameters of both the projector and the camera are studied, such as the gamma function and the responsivity of the sensor. Besides, the reflectance of different objects is measured and added to the analytical model of the technique.

The influence of color on the behavior of the combination projector-camera is analyzed by the coupling matrix of the sensor, which yields the level of overlapping of the primary colors in both the response of the projector and the camera [40]. In addition to digital projectors, other light sources are investigated: a blue laser, infrared LEDs, red LEDs, UV LEDs and a sodium lamp.

In the end, two optimized setups are presented. Both involved the incorporation of independent light sources for each technique. An advantage of having two independent light sources is that the intensity and projection angle of the DIC source can be appropriately selected in accordance with roughness, color and dynamic range of the object. The first setup deals with neutral-colored objects; in this case, the best combination of light (one light source for DIC and another for FP) resulted to be a matrix of red LEDs for DIC (uniform light beam) and blue light from a projector, for FP (one part of the fringe is blue and the rest is black). This result was expected since blue and red are largely separated in the sensitivity spectral curve of the sensor and therefore show the least overlapping. The second optimized setup is implemented for the case of multi-colored objects. In these conditions, the light combination with the highest performance is the following: for DIC, a matrix of UV LEDs (background uniform light), and for FP, blue light from a projector (one portion of the fringe is blue and the other is black).

The multi-colored objects are composed of various representative colors, for example red, green, blue, yellow, black, gray, and white. Black and white stripes are added to the scene in order to evaluate the performance of the technique when large-dynamic range scenes are involved. We found that even under high-dynamic range scenes, the technique maintains relatively high accuracy on the results.

The viability of the technique is shown by measuring three-dimensional displacement in two practical experiments: behavior of the free surface of a geological model constituted by several layers of sand when subjected to external compression, and the displacement dynamics of an avalanche produced by throwing a load of sand

along an inclined plane of 1-m length. The first experiment helps us understand the mechanism of formation of the principal bodies found on the earth's crust, such as all types of natural ridges and faults. Likewise, through the second experiment we can get some insight into the dynamics of landslides, phenomenon that generally causes large damages to structures located on its trajectory.

The work is organized as follows. In Chapter 2, the theory of FP and DIC is presented. Then, Chapter 3 is dedicated to the optimization and the feasibility of the combined method, FP-DIC (a white object is assumed). Following, the analysis of multi-colored objects is given in Chapter 4. Some applications of the proposed technique are included in Chapter 5. And finally, in Chapter 6, we draw our conclusions of the work and comment on some further investigations that may be done in the future.

1.1 References

1. R. Jones and C. Wykes, *Holographic and speckle interferometry*, 2nd Ed., Cambridge University Press, Cambridge (2009).
2. D. Malacara, *Optical Shop Testing*, 3rd Ed., John Wiley and Sons, New Jersey, USA (2007).
3. D. W. Robinson, *Interferogram analysis (digital fringe pattern measurements),* IOP Publishing Ltd., Philadelphia (1993).
4. K. J. Gasvik, *Optical Metrology*, 3rd Ed., John Wiley and Sons, Sussex, UK (2003).
5. M. Raffel, C. Willert, and J. Kompenhans, *Particle image velocimetry, a practical guide*, Springer, New York (1998).
6. R. Weller and B. M. Shepperd, "Displacement measurement by mechanical interferometry," Proc. Soc. Exp. Stress. Anal. (SESA), **6**(1), 35-38 (1948).
7. S. H. Rowe and W. T. Welford, "Surface topography of non-optical surfaces by projected interference fringes," Nature, **216**, 786-787 (1967).
8. D. M. Meadows, W. O. Johnson, and J. B. Allen, "Generation of surface contours by moiré patterns," App. Opt., **9**(4), 942-947 (1970).
9. B. Dessus, M. Leblanc, "The 'fringe method' and its application to the measurement of deformations, vibrations, contour lines and differences of objects," Optoelectronics 5, 369-391 (1973).
10. G. Indebetouw, "Profile measurement using projection of running fringes," App. Opt., **17**(18), 2930-2933 (1978).
11. M. Takeda, H. Ina, and S. Kobayashi, "Fourier-transform method of fringe –pattern analysis for computer-based topography and interferometry," JOSA, **72**(1), 156-160 (1982).
12. V. Srinivasan, H. C. Liu, and M. Halioua, "Automated phase-measuring profilometry of 3-D diffuse objects," App. Opt., **23**(18), 3105-3108 (1984).
13. A. K. Asundi, "Moiré methods using computer-generated gratings," **32**(1), Opt. Eng., 107-116 (1993).
14. B. Barrientos, M. Cywiak, W. K. Lee, and P. Bryanston-Cross, "Measurement of dynamic deformation using a superimposed grating," Rev. Mex. Fis. **50**(1), 12-18 (2004).
15. J. M. Burch and J. M. J. Tokarski, "Production of multiple beam fringes from photographic scatterers," Optica Acta, **15**, 101-111 (1968).
16. N. A. Fomin, *Speckle photography for fluid mechanics measurements*, Springer, Berlin (1998).
17. M. Raffel, C. Willert, and J. Kompenhans, *Particle image velocimetry*, Springer, Berlin (1998).
18. W. H. Peters and W. F. Ranson, "Digital imaging techniques in experimental stress analysis," Opt. Eng., **21**, 427-431 (1981).

19. T. C. Chu, W. F. Ranson, M. A. Sutton, "Applications of digital-image-correlation techniques to experimental mechanics," Exp. Mec., **25**(3), 232-244 (1985).
20. M. A. Sutton, W. J. Wolters, W. H. Peters, W. F. Ranson, and S. R. McNeill, "Determination of displacements using an improved digital correlation method," Ima. and Vision Comp., **1**(3), 133-139 (1983).
21. B. Pan, K. Quian, H. Xie, and A, Asundi, "Two-dimensional digital image correlation for in-plane displacement and strain measurement: a review," Meas. Sci. Technol., **20**, 062001 (2009).
22. C. Quan, C. J. Tay, and Y. H. Huang, "3-D deformation measurement using fringe projection and digital image correlation," Optik, **115**(4), 164-168 (2004).
23. T. N. Nguyen, J. M. Huntley, R. Burguete, and C. R. Coggrave, "Combining digital image correlation and projected fringe techniques on a multi-camera multi-projector platform," J. Physiscs, 7th International Conference on Modern Practice in Stress and Vibration Analysis, **181**, 012076 (2009).
24. B. Barrientos, M. Cerca, J. García-Márquez, and C. Hernandez-Bernal, "Three-dimensional displacement fields measured in a deforming granular-media surface bycombined fringe projection and speckle photography," J. Opt. A: Pure Appl. Opt., **10**, 104027 (2008).
25. H. Weber, R. Lichtenberger, and T. Wolf, "The combination of speckle correlation and fringe projection for the measurement of dynamic 3-D deformations of airbags caps," in *Proceedings of IUTAM Symposyum on Advanced Optical Methods and Applications in Solid Mechanics*, A. Lagarde, ed. (Kluwer Akademic Publishers, 2000), pp. 619–626.
26. C. J. Tay, C. Quan, T. Wu, and Y. H. Huang, "Integrated method for 3-D rigid-body displacement measurement using fringe projection," Opt. Eng., **43**(5), 1152-1159 (2004).
27. P. Siegmann, V. Alvarez-Fernandez, F. Diaz Garrido, and A. E. Patterson, "A simultaneous in- and out-of-plane displacement measurement method," Opt. Lett. **36**(1), 10–12 (2011).
28. Z. Zhang, "Time efficient color fringe projection system for 3D shape and color using optimum 3-frequency selection," Opt. Exp. **14**(14), 6444-6455 (2006).
29. L. Fu, Z. Li, L. Yang, Q. Yang, and A. He "New phase measurement profilometry by grating projection," Opt. Eng. **45**(7), 073601-4 (2006).
30. H. G. Park, D. Dabiri, and M. Gharib, "Digital particle image velocimetry/thermometry and application to the wake of a heated circular cylinder," Exp. Fluids **30**, 327-338 (2001).
31. Ch. Brucker, "3-D PIV via spatial correlation in a color-coded light-sheet," Exp. Fluids **21**, 312-314 (1996).
32. C. Wust and D. W. Capson, "Surface profile measurement using color fringe projection," Mach. Vis. App. **4**, 193–203 (1991).
33. P. S. Huang, Q. Hu, F. Jin, and F. P. Chiang, "Color-encoded digital fringe projection technique for high-speed three-dimensional surface contouring," Opt. Eng. **38**(6), 1065–1071 (1999).
34. J. L. Flores, J. A. Ferrari, G. Garcia-Torales, R. Legarda-Saenz, and A. Silva, "Color-fringe pattern profilometry using a generalized phase-shifting algorithm," Appl. Opt. **54**(30), 8827–8834 (2015).
35. M. Padilla, M. Servin, and G. Garnica, "Fourier analysis of RGB fringe-projection profilometry and robust phase-demodulation methods against crosstalk distortion," Opt. Express **24**(14), 15417–15428 (2016).
36. I. Trumper H. Choi, and D. W. Kim, "Instantaneous phase shifting deflectometry," Opt. Express, **24**(24), 27993–28007 (2016).
37. P. Synnergren and M. Sjodahl, "A stereoscopic digital speckle photography system for 3-D displacement field measurements," Opt. Lasers Eng. **31**, 425-443 (1999).
38. A. K. Prasad, "Stereoscopic particle image velocimetry," Exp. Fluids **29**, 103-116 (2000).
39. C. Mares, B. Barrientos, and A. Blanco, "Measurement of transient deformation by color encoding," Opt. Express **19**, 25712–25722 (2011).
40. C. Mares, B. Barrientos, and R. Valdivia, "Three-dimensional displacement in multi-colored objects," Opt. Express, **25**(10), 11652–11672 (2017).

2 Theory

In Chapter 1, it has been mentioned that combining digital image correlation (DIC) and fringe projection (FP) may be adequate for the simultaneous measurement of the three components of deformation in solid objects [1, 2]. In general, a complete characterization of displacement fields must contain the 2-D in-plane displacement components and the out-of-plane component. The two mutually perpendicular in-plane components of displacement are obtained by the correlation technique whereas the out-of-plane component is addressed by fringe projection. In both techniques, two images of the object for two different states are captured (reference image and displaced image, respectively). As the object undergoes deformation, the corresponding spatial structures carrying the information (variations of intensity of the object surface in the case of digital correlation and fringes in fringe projection) move accordingly transversally. In FP, the transverse displacement of the fringes is done via the Fourier transform phase method, and in DIC, via correlation. Thus, it is possible the calculation of displacement fields by comparing the reference image and the displaced image.

2.1 Fringe projection, FP

Fringe projection is a valuable tool for the calculation of out-of-plane displacements such as those involved in vibration analyses [3]. In this case, by the aid of a projector, a pattern with straight fringes is projected onto the surface of an object. A schematic of an optical arrangement for FP is shown in Fig. 1. The camera captures images of the object surface as deformation is applied. For a reference state, assuming a plane object, the fringes may deviate from straightness due to projection effects and optical aberrations of the imaging lens. If these effects are assumed to remain constant for both the deformed image and the reference image, then they can be readily compensated by subtracting the corresponding phases. As the object undergoes deformation, the out-of-plane component of displacement makes the fringes depart further from straightness. Deviations from straightness of the fringes may be up to several periods of the projected grating. The lateral deviation from straightness $\Delta x(x,y)$ for each point (x,y) is related directly with the change of phase $\Delta\phi(x,y)$ by $\Delta x = T\Delta\phi/2\pi,$ with T being the period of the grating, which is taken as

constant for a telecentric system; from Fig. 1 we can see that the out-of-plane displacement component is given by

$$\Delta z = D\Delta x / \left(B + \Delta x\right) \approx \Delta x / \tan\alpha, \qquad (2.1)$$

where $\alpha = \tan^{-1}(B/D)$ is the projection angle; normal observation is considered as well as shown in Fig. 2.1. By introducing an equivalent period $T_0 = T/\tan\alpha$, the last equation can be rewritten as $\Delta z = T_0 \Delta\phi / 2\pi$.

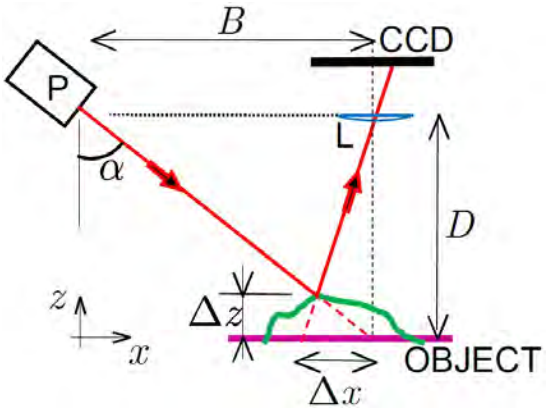

Fig. 2.1. Schematic layout of FP. Here P and L stand for projector and imaging lens, respectively. Other variables are described in the text.

The change of phase $\Delta\phi$ can be calculated via the Fourier method [4] as follows. Let the reference image be expressed by [5]

$$I_1(x,y) = a(x,y) + b(x,y)\cos\left(2\pi f_0 x + \phi_{ref}\right), \qquad (2.2)$$

where $a\left(x,y\right)$ is the background illumination, $b\left(x,y\right)$ the modulation term of the fringes, f_0 is a carrier frequency that allows us the use of the Fourier method for automatic phase calculation ($f_0 = 1/T$), and ϕ_{ref} a phase term that accounts for projection and aberration effects. Likewise, the displaced image may be defined by

$$I_2(x,y) = a(x,y) + b(x,y)\cos\left(2\pi f_0 x + \phi_{ref} + \Delta\phi\right). \qquad (2.3)$$

The arguments of Eqs. (2.2) and (2.3) can be calculated by the Fourier method. For example, for the reference image, after applying the Fourier transform operator we obtain

$$I_F(f_x,f_y) = A(f_x,f_y) + B(f_x - f_0,f_y) + B^*(-f_x - f_0,f_y), \tag{2.4}$$

where $A\left(f_x,f_y\right) = \Im\left\{a\left(x,y\right)\right\}$ and $B\left(f_x,f_y\right) = \Im\left\{\frac{1}{2}b\left(x,y\right)\exp\left(i2\pi f_0 x\right)\exp\left(i\phi_{ref}\right)\right\}$. The asterisk denotes the operation of complex conjugation. The Fourier transform operator is indicated by $\Im\{\ \}$ and the frequency domain variables by $\left(f_x,f_y\right)$.

Now, we apply the inverse Fourier transform to a band-pass filtered version of Eq. (2.4), which contains only one of its spectrum side lobes (this lobe is centered at the carrier frequency f_0),

$$\begin{aligned}\Im^{-1}\left\{B(f_x - f_0,f_y)\right\} &= \Im^{-1}\left\{\Im\left\{\frac{1}{2}b(x,y)\exp(i2\pi f_0 x)\exp\left(i\phi_{ref}\right)\right\}_{f_x - f_0, f_y}\right\} \\ &= \mathrm{Re}(x,y) + i\ \mathrm{Im}(x,y),\end{aligned} \tag{2.5}$$

where $\mathrm{Re}(x,y) = \frac{1}{2}b(x,y)\cos\left(2\pi f_0 x + \phi_{ref}\right)$ and $\mathrm{Im}(x,y) = \frac{1}{2}b(x,y)\sin\left(2\pi f_0 x + \phi_{ref}\right)$. Therefore, the reference argument can be obtained by

$$2\pi f_0 x + \phi_{ref} = \tan^{-1}\frac{\mathrm{Im}(x,y)}{\mathrm{Re}(x,y)}. \tag{2.6}$$

In a similar way, the argument of the displaced image $\left(2\pi f_0 x + \phi_{ref} + \Delta\phi\right)$ can be calculated; the desired phase term can be finally found by subtracting directly the latter two arguments or alternatively by [6]

$$\Delta\phi\left(x,y\right) = \tan^{-1}\left(\frac{\mathrm{Im}_2\,\mathrm{Re}_1 - \mathrm{Im}_1\,\mathrm{Re}_2}{\mathrm{Re}_1\,\mathrm{Re}_2 + \mathrm{Im}_1\,\mathrm{Im}_2}\right), \tag{2.7}$$

where subscripts 1 and 2 correspond to the reference and displaced images, respectively.

To consider the intrinsic projection variations of the projected grating, a compensation factor may be applied to the period measured at the center of the field of view [5], $T = 1/f_0$, as $T' = T\left(1 + x\sin\alpha / l\right)^2$, where α is the mean angle between projector and the optical axis of the camera (as depicted in Fig. 2.1), and l represents the distance between the exit of the light source and object. The out-of-plane displacement Δz can be obtained by [5] [instead of Eq. (2.1)]

$$\Delta z = \frac{\Delta\phi}{2\pi}\frac{T'\cos\alpha}{\sin\alpha + (D - l\cos\alpha)x/(lD)}. \qquad (2.8)$$

Phase maps calculated by Eq. (2.7) may give rise to wrapped phase maps when absolute difference-of-phase values are larger than 2π rad. To remove the resulting phase jumps, a simple unwrapping algorithm can be applied,

$$\phi_{m_0,n} = \phi_{m_0,n-1} + \tan^{-1}\left[\tan\left(\psi_{m_0,n} - \phi_{m_0,n-1}\right)\right], \qquad (2.9)$$

where ψ and ϕ are wrapped and unwrapped phases, respectively; m and n are integer dummy indices that run from 0 to $M-1$ and $N-1$, with MxN being the size of the images. Also, m_0 refers to the initial row for unwrapping, with $\phi_{m_0,0}$ generally taken as 0. The latter equation allows us to unwrap just one row of the wrapped phase image. To unwrap the complete phase image, column-wise unwrapping can be used,

$$\phi_{m,n} = \phi_{m-1,n} + \mathrm{atan}\left[\tan\left(\psi_{m,n} - \phi_{m-1,n}\right)\right].$$

In this case, $\phi_{m_0,n}$ corresponds to the values given by Eq. (2.9).

2.2 Digital image correlation, DIC

The optical arrangement for DIC is identical to the one used for FP, shown in Fig. 1. To discard any intrusive effect that may result from surface preparations, like surface spraying or painting, the object is illuminated uniformly so that the speckle signal of the DIC images is formed by the natural texture of the object surface.

An image of the surface texture (white-light speckle) of an object illuminated by white light serves as the carrier signal for DIC. By taking two images of the object by a CCD camera, before and after deformation, the relative displacement between these images can be found by cross correlating corresponding subimages [7, 8]. Take $I_2(x,y)$ and $I_1(x,y)$ as the distributions of intensity of the reference and displaced subimages, respectively; then, we may assume that $I_2(x,y) = I_1(x-\Delta x, y-\Delta y)$; relative displacements $(\Delta x, \Delta y)$ may be determined by the two-dimensional correlation function defined as

$$h(\Delta x,\Delta y) = \int_{-\infty}^{\infty}\int_{-\infty}^{\infty} I_1(x,y) I_1(x-\Delta x, y-\Delta y)\, dx\, dy, \qquad (2.10)$$

which in turn may be obtained by the Fourier transform,

$$h(\Delta x,\Delta y) = \Im^{-1}\left\{F_1(f_x,f_y) F_2^*(f_x,f_y)\right\}, \qquad (2.11)$$

where, $F_1(f_x,f_y)$ and $F_2(f_x,f_y)$ denote the Fourier transform of $I_1(x,y)$ and $I_2(x,y)$, respectively. The coordinates of the location of the maximum of the correlation map, $h(\Delta x,\Delta y)$, correspond directly to the desired in-plane displacements. Subpixel resolution in the calculation of displacements can be achieved by fitting Gaussian [7] or paraboloidal [8] functions to the values defining the correlation distribution surrounding the main peak of correlation.

2.3 Conclusions

Fringe projection and digital image correlation are techniques that are implemented by the same optical setup. Besides, they also allow a similar range of measurement, from 20 micrometers, roughly, to a few centimeters. Both of them use white light for illumination, which can be spatially structured. Considering these similar features, it is natural to try to use them in combination.

Both techniques have their roots in classical older techniques. FP was developed from moiré techniques and DIC from speckle photography.

2.4 References

1. C. J. Tay, C. Quan, T. Wu, and Y. H. Huang, "Integrated method for 3-D rigid-body displacement measurement using fringe projection," Opt. Eng. **43**(5), 1152-1159 (2004).
2. B. Barrientos, M. Cerca, J. Garcia-Marquez, and C. Hernandez-Bernal, "Three-dimensional displacement fields measured in a deforming granular-media surface by combined fringe projection and speckle photography," J. Opt. A: Pure App. Opt. **10**, 104027, 10 pp (2008).
3. B. Barrientos, M. Cywiak, W. K. Lee, and P. Bryanston-Cross, "Measurement of dynamic deformation using a superimposed grating," Rev. Mex. Fis. **50**(1), 12-18 (2004).
4. M. Takeda, H. Ina, and S. Kobayashi, "Fourier-transform method of fringe-pattern analysis for computer-based topography and interferometry," JOSA A **72**(1), 156-160 (1982).
5. K. J. Gasvik, *Optical Metrology*, (3rd Ed. John Wiley and Sons, Sussex 2003).
6. T. Kreis, "Digital holographic interference-phase measurement using the Fourier-transform method," JOSA A **3**(6), 847-855 (1986).
7. M. Raffel, C. Willert, and J. Kompenhans, *Particle image velocimetry, a practical guide*, (Springer-Verlag, Berlin, 1998).
8. D. J. Chen, F. P. Chiang, Y. S. Tan, and H. S. Don "Digital speckle-displacement measurement using a complex spectrum method," App. Opt. **32**(11), 1839-1849 (1993).

3 Feasibility of simultaneity of FP-DIC

In this chapter we develop the characteristics of the proposed FP-DIC system, such as the optimal parameters of the system. Along with this, we analyze the influence of the residual signals related to each technique on the overall performance of FP-DIC. The principal aim of this part is to show the viability of the technique to be used for studies of transient events.

3.1 One-shot method, FP-DIC

For the analysis of deformation of relatively fast phenomena, such as vibration studies, it is desirable that one image contain all the necessary information for the measurement. This may be fulfilled by combining DIC and FP. To register simultaneously the signals for both techniques, an image with cyan stripes (a combination of blue and green, with RGB values of [0,255,255]) embedded in a white background [255,255,255] is considered. A computer-generated structured pattern considering this idea is shown in Fig. 3.1(a). This pattern is to be projected onto the object under test. The ratio of the cyan part to the white part of each fringe is assumed to be 0.25.

The resulting illuminating spatial pattern corresponds to a binary grating, instead of a sinusoidal type as required by Eqs. (2.2) and (2.3). However, this fact does not change the theory given above since any harmonic side lobes can be filtered out readily when applying the band-pass filter in the Fourier method. Furthermore, when considering the optical transfer functions of the involved optical components (projector, imaging lens and camera sensor), the obtained profile of the fringes departs from being squared and look a bit as sinusoidal, see the red plot in Fig. 3.1(d) where an equivalent grating period T_0 of 1.93 mm is used.

With a white-painted object, the surface texture information appears on the blue channel since the blue region of the projected image presents a similar intensity to that of the white region, and hence no fringes result. Unlike this, fringe information appears on the red channel as the cyan portion of the projected image is blocked and therefore appears black. As the white portion of the projected image results with nonzero intensity then a pattern of binary fringes results (after digital separation), see Fig. 3.1(e).

In Fig. 3.1(b) we present the registered image by the camera. After digital separation of the signals from the three color channels, the corresponding image for the blue channel is obtained, as shown in Fig. 3.1(f). Cross sections of the Fourier transform of images 3.1(e) and 3.1(f) are shown in Fig. 3.1(g). As observed, a residual signal at the carrier frequency is present in the blue image. If the strength of this signal becomes significant it could affect the in-plane measurements. In the results presented below this was not the case.

As noted from Fig. 3.1(b), in the registered image, the white part of the fringes acquires a greenish hue. This effect arises from the mechanisms of color balancing of the camera and it increases as the grating pitch decreases. Cross sections of Figs. 3.1(a) and 3.1(b) are shown in Figs. 3.1(c) and 3.1(d). As it is noticed, despite the large departure between the computer-generated and the registered images, measurements with enough accuracy can be done.

In Fig. 3.2 we show another example but with an equivalent period of 9.90 mm. As it is observed, the white part of the fringe, despite being larger than before, also acquires a bluish hue because of artifacts of the camera (by design, the camera tries to automatically adjust the white balance, even when the manual setting is selected. This issue should be addressed correctly by other camera models). For better results in this case, the cyanide color was set as [0,255,200]. By observing Fig. 3.2(f), it may be apparent that the blue value may be lowered further in order to reduce the observed residual fringes in the speckle image, but the camera in that case starts yielding distorted images —In Section 3.3, the components of the experimental setup is described. Results of the accuracy of the method as a function of the equivalent period are discussed in Section 3.3 as well.

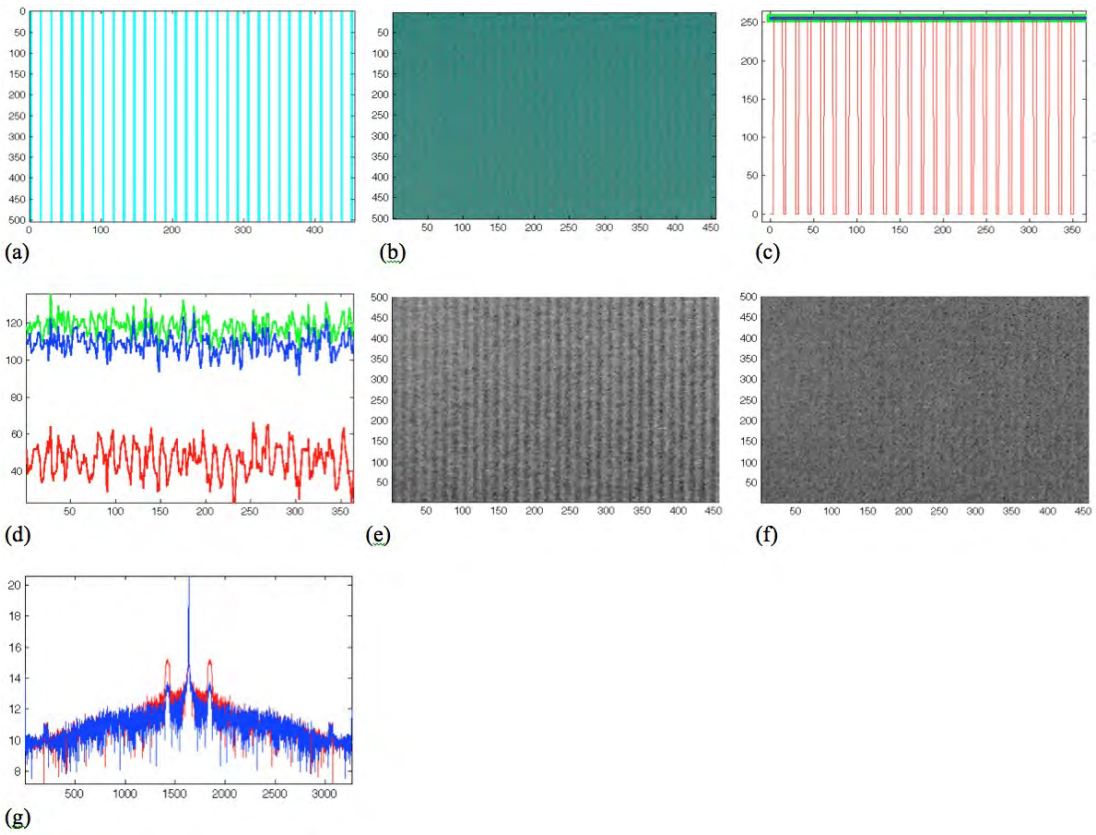

Fig. 3.1. (a) Computer-generated image (subimage of the original image of 3264x2448 pixels). (b) Recorded image (subimage of the recorded image of 3264x2448 pixels). (c) and (d) Cross-sections of the two previous images (RGB components) along x-direction (center row). After color separation, detected signals on (e) red channel and (f) blue channel. (g) Cross-sections of the Fourier transform of the last two images (full versions). Colors indicate the corresponding channel. An equivalent period of 1.93 mm was used. Dimensions: abscissae and ordinates in pixels, except ordinates in (c) and (d) (in gray levels) and (g) (arbitrary units).

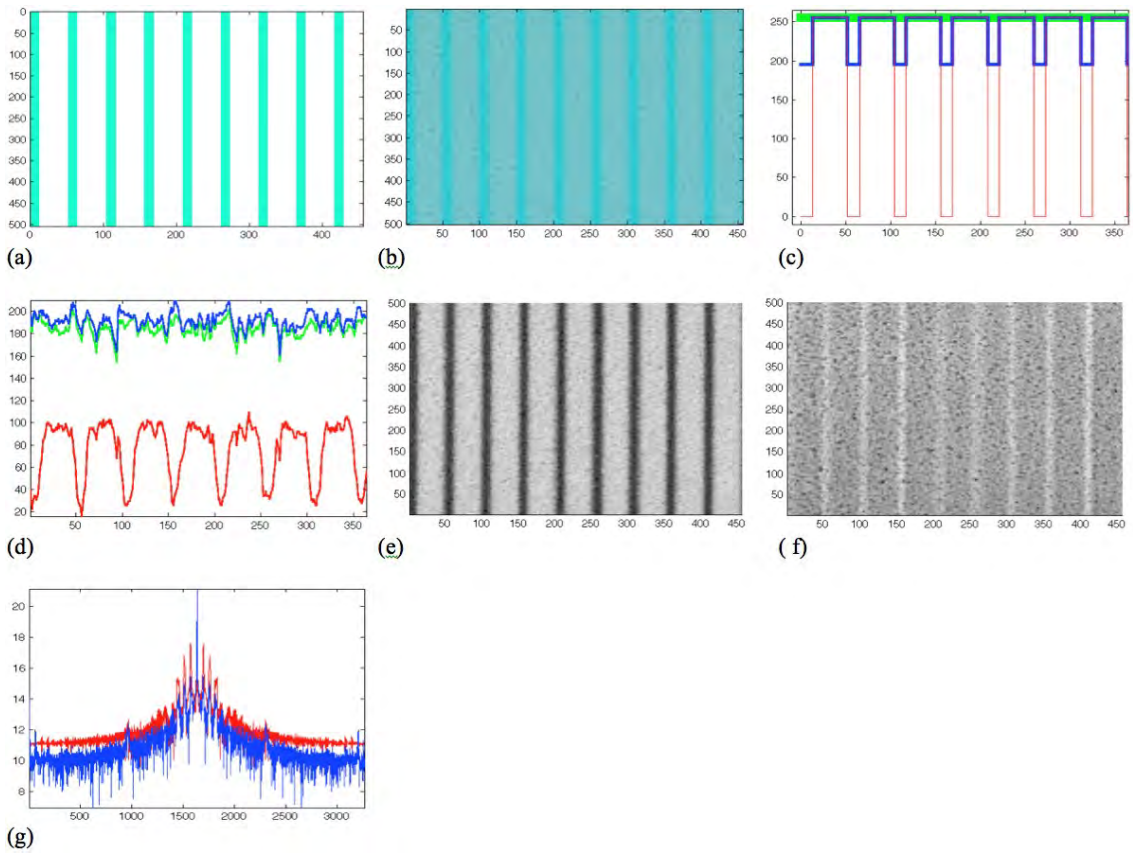

Fig. 3.2. Equivalent period of 9.90 mm. Titles of figures are as the corresponding ones in Fig. 3.1.

For colored objects, partial absorption of the illuminating light occurs and contrast of the signals for FP and DIC is expected to decrease. This may imply a reduction of the accuracy of the proposed method. Complete analysis of this issue should have to take into account the spectral characteristics of the projector, the coupling effects between neighboring channels and the color characteristics of the object [1]. This type of analysis is the subject of Chapter 4.

A preliminary example of a neutral-colored object is shown in Fig. 3.3. Images in this figure are described as in Fig. 3.2. The mean color of the object when illuminated by white light is [190,93,110], see Fig. 3.3(h). For neutral-colored objects, selection of the illuminating light should take into account the color content of the object. For the current example we use illuminating light formed by green fringes [0,255,60] embedded in a magenta background [127,0,255]. As noticed from Figs. 3.3(e) and 3.3(f), the separation of the signals is still possible. However, for some particular colors, such as pure red hues, the method is not adequate and the theory should be extended, as described in Chapter 4.

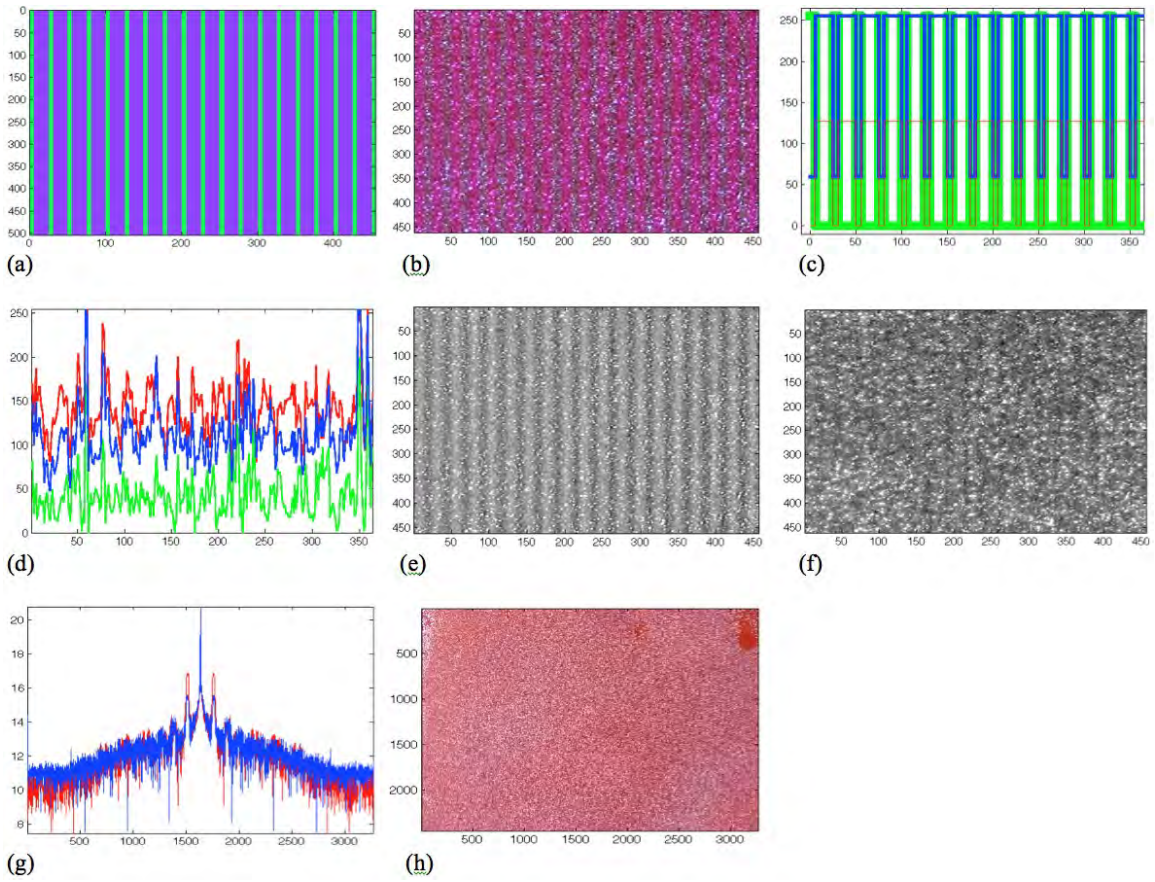

Fig. 3.3. Equivalent period of 2.83 mm. Titles of figures (a)-(g) are as the corresponding ones in Fig. 3.2. (h) Object illuminated by white light.

3.2 Influence of residual speckle on the accuracy of FP

When particles (white-light speckles) are directly painted on the object as in Ref. 2, they ultimately appear in the fringe image as multiplicative noise. This effect may be represented as a random variation of the object reflectance $r(x,y)$. Thus, the intensity recorded by the camera for a certain object state can be expressed as [3]

$$I_2(x,y) = r(x,y)\left[a(x,y) + b(x,y)\cos\left(2\pi f_0 x + \phi_{ref} + \Delta\phi\right)\right]. \quad (3.1)$$

In our case, the representation of fringe images with residual white-light speckles follows that given by Eq. (3.1) as well, but the contrast of the speckle is relatively low. When applying the Fourier method to Eq. (3.1), the expression for the band-pass filtered side lobe in the Fourier domain, Eq. (2.5), should be modified to consider high-frequency components of the central lobe that may permeate into the

side lobe. In this case, recovering of the phase term is not warranted. However, if Eq. (2.5) is used with no modification, a reduction of the accuracy of FP results. An additional source of error for the Fourier method arises from the digitalization of the high-frequency signals that constitutes the speckle field. This problem has been previously pointed out in [4].

To show the influence of the white-light speckle on the FP accuracy, we carry out numerical simulations by using Eq. (2.4) with the following values: $a(x,y)=1$, $\phi_{ref}=0$, $\Delta\phi=4\pi(x^2+y^2)$ with $x,y\le|1/2|$ and $f_0=64$. The object reflectance is expressed as a summation of Gaussian functions, $r'(x,y)=\sum_{n=1}^{N}\exp\left\{-2\left[(x-x_n)^2+(y-y_n)^2\right]/\sigma^2\right\}$, whose centers (x_n,y_n) are randomly selected, and have constant radii σ. By varying the latter parameter and the number of Gaussian functions N, the level of disturbance caused by the residual speckle field can be adjusted. Furthermore, adjustment of the speckle contrast can be achieved by considering a normalized version of $r'(x,y)$, $r(x,y)=\left[norm\left\{r'(x,y)\right\}\right]B+A$, where $norm\{\cdot\}$ denotes a normalization operator and A and B the background and the contrast of the speckle field (with $A+B=1$), respectively. Thus, the resulting effect caused by the residual speckles can be varied by either N, σ, A, B, or by any combination of them.

The aspect of the simulated images with fringes can be altered as well by changing the modulation term $b(x,y)$. For relatively small fringe modulation the influence of the speckle field is enhanced. In Fig. 3.4 we show three simulated displaced images; N is taken as 2×10^6. Numerical simulations are done in Matlab Version 7. The reference image is not shown, but is also obtained from Eq. (3.1) with $\Delta\phi=0$. Figure 3.4(a) corresponds to a speckle-free image with $b(x,y)=1$, while figures 3.4(b) and (c) to images with speckle content; for Fig. 3.4(b), we set $\sigma=2.0/S$, where $S=1024$ pix (the size of the image; here pix stands for pixel), $b(x,y)=0.12$, and $A=0.6$; and for Fig. 3.4(c), $\sigma=3.0/S$, $b(x,y)=0.05$, and $A=0.65$. For these two last cases, modulation $b(x,y)$ is measured directly from the experimental images shown in Figs. 3.4(d) and (e), respectively. Calculation of $b(x,y)$ is done by using Eq. (2.5) as

$$b(x,y)=2\left|\mathrm{Re}(x,y)+i\,\mathrm{Im}(x,y)\right|. \qquad (3.2)$$

The percentage relative errors of the phase, for the synthetic images, Figs. 3.4(a)-(c), after applying the Fourier method, are 0.1, 1.6 and 3.6%, respectively. These values are calculated by

$$pre = \frac{\sqrt{\sum_{m=1}^{M}\sum_{n=1}^{N}\left[\left(\phi_o\right)_{mn} - \left(\phi_r\right)_{mn}\right]^2}}{\max\left[\left(\phi_o\right)_{mn}\right]} \times 100, \qquad (3.3)$$

where $\left(\phi_o\right)_{mn}$, $\left(\phi_r\right)_{mn}$ are the given and recovered values, respectively, and $\max\left[\left(\phi_o\right)_{mn}\right]$ is the maximum value of the given phase.

As expected, the accuracy of the FP method varies inversely with the contrast of the speckle field and directly with the modulation of the fringe pattern. Recently, a similar result has been found for fringe projection using laser interference [5].

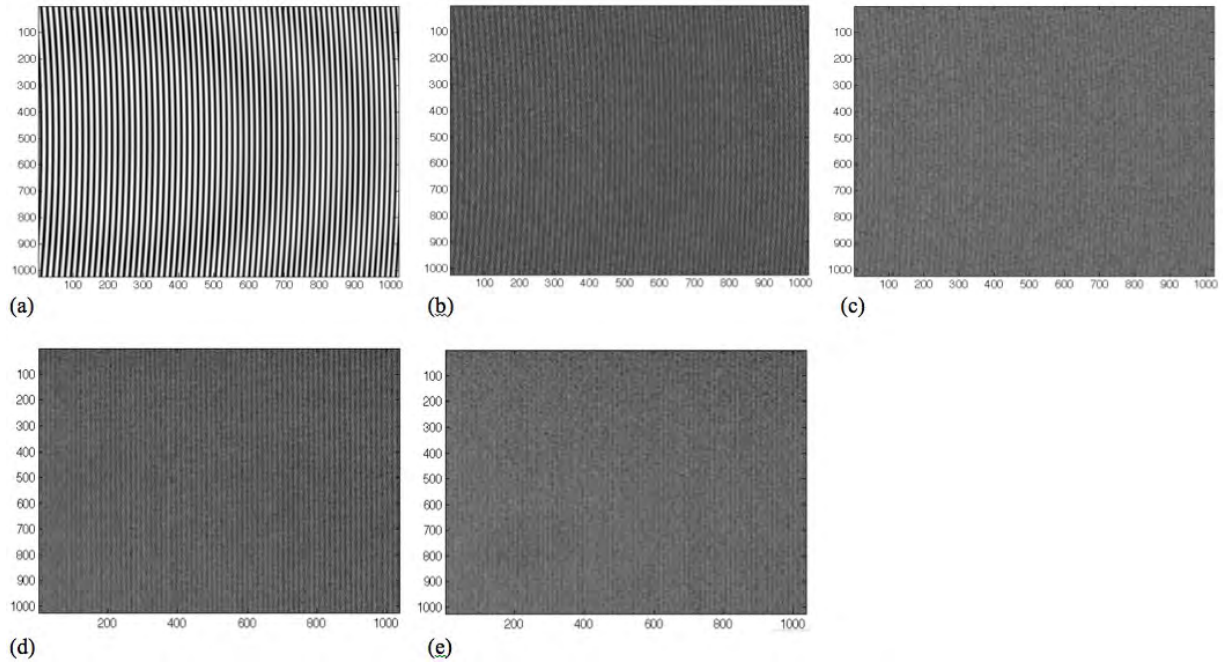

Fig. 3.4. Synthetic images used to show the influence of residual speckle on the accuracy of the FP method: (a) Speckle-free fringe image, (b) and (c) fringe images with different level of speckle disturbance. Experimental images: (d) and (e), images with similar speckle influence to (b) and (c), respectively. Dimensions are pixels.

As described in the next section, experimental cases resembling images in Figs. 3.4(b) and 3.4(c), occur when small projected periods are used; e.g., Figs. 3.4(d) and 3.4(e), respectively. In that case, the object texture affects significantly

the contrast of the projected fringes. In both Figs. 3.4(d) and 3.4(e), a projected period of 0.78 mm is used, but the roughness in 3.4(e) is larger than in 3.4(d). The calculated relative errors for these two cases are 2.6% and 7.0%, respectively. The complete measurement of experimental errors is given in the following section, where the roughness of the object is maintained unchanged and corresponds to the case illustrated in Fig. 3.4(d).

3.3 Experimental results

For the experimental results, the arrangement employed for DIC and FP is illustrated in Fig. 3.5. It consists of a high-definition three-LCD Panasonic projector (PT-AE2000U, 1500 lm) and an Olympus camera (Camedia C8080WZ, 2/3" Bayer mosaic-based CCD sensor, 8 Mpix) which renders images of 3264x2448 pix. The imaging system is set to an f-number of 3.5 and exposure time of 1/1000 s. Distances from the object to projector and from the camera to projector are selected as to minimize projection effects [6]. Also, the projection angle is set to 22° and the projected period is selected to take on the values: 0.78, 1.00, 2.00, 3.00 and 4.00 mm (corresponding equivalent periods of 1.93, 2.48, 4.95, 7.43 and 9.90 mm). The object is an aluminum plate of dimensions 300x300x6.35 mm whose surface is sprayed white by applying a powder developer (Ardrox 9D4A). The width of the region of observation is not constant: 164, 170 and 250 mm; the first value corresponds to the first value of the projected period of 0.78 mm, the second value to period 1.0 mm, and the last value to periods 2.0, 3.0 and 4.0 mm. The three main components of the layout, CCD camera, object and projector, are mounted on tripods as shown in Fig. 3.5(a). Figure 3.5(b) represents a schematic diagram of the setup. Care was taken in the alignment of the experimental setup, in particular to prevent the appearance of any significant in-plane displacement when the object is given an out-of-plane displacement, and similarly for given in-plane displacements.

The experiment consists in translating the aluminum plate by known steps along the three coordinate axes. The steps are given by a translation stage driven by a step-motor, from Thorlabs, with 1.25 micrometers per step. For each projected period, the aluminum plate is given the following displacements in mm (out-of-plane and in-plane displacements): 0.063, 0.125, 0.250, 0.500, 0.750, 1.000, 1.250, 1.500, 1.750 and 2.000, which in pixels are (for $T = 1.0$mm) 0.8, 1.6, 3.3, 6.5, 9.8, 13.1, 16.3, 19.6, and 26.1. In Fig. 3.5(c) we show a typical image

produced by the system when the illuminating light corresponds to a pattern of black-and-white stripes.

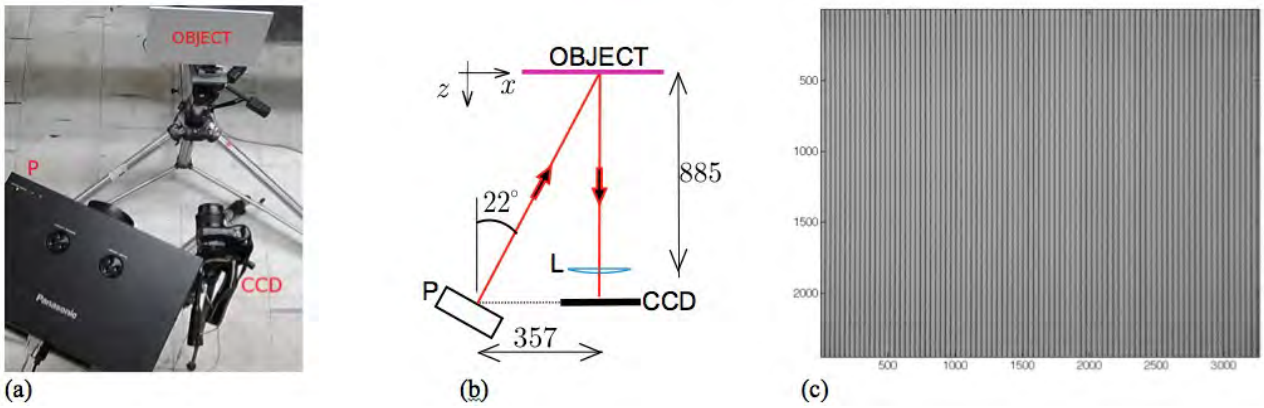

Fig. 3.5. Optical layout. (a) Photograph. (b) Schematic drawing. Dimensions are mm. (c) Typical image obtained when illuminating the object with black-and-white fringes. Dimensions are pixels. Symbols are as in Fig. 2.1.

In Fig. 3.6 we show results of the obtained accuracy of the method for the five different grating periods, for both out-of-plane and in-plane displacements. For each given displacement, three measurements were done, and the average relative error is calculated. In addition to this, results using standard methods for FP and DIC are included and are indicated by letters BW. These standard results were obtained by projecting black-and-white fringes for FP and uniform white light for DIC, and serve as reference values. The reference measurements were implemented in a non-simultaneous way.

On calculation of in-plane displacements, software for correlation of images from IDT (proVISION-XS) is used. A subimage size of 64x64 pix is used. It is worth noting to point out that when calculating out-of-plane displacements, phase unwrapping is not required as all the equivalent periods are greater than the displacements (an exception case is the displacement of 2.0 mm combined with an equivalent period of 1.931 mm). Besides, the duty cycle of the period was set to 75%, in order to reduce the size of the region that is partially darkened by the cyan portion of the fringes, which may affect the speckle information.

From Fig. 3.6 it is observed that the overall performance of DIC is greater than that of FP, for the present conditions. This result was found in previous works as well [7, 8]. From Fig. 3.6(a), we see that the accuracy obtained for both small and

large out-of-plane displacements is high in the case of small grating periods (case of $T = 1.0\,\text{mm}$). It would be expected that the smallest period, $T = 0.78\,\text{mm}$, give still better results, but the discrepancies between the given and the measured displacements rather increase. This is due to the fact that a notable reduction of the contrast of the fringes occurs when the camera lens gets close to its resolving limit. Additionally, as the period increases, the error increases on average slightly. Notice also the reliability of the proposed method by comparing the relative errors obtained by the standard method (labeled by BW) and by the proposed method. For the reference results, periods of 1.00 and 4.00 mm were used —indicated by 1.00 BW and 4.00BW in Fig. 3.6(a), respectively.

On the other hand, from Fig. 3.6(b), it is seen that the in-plane error is relatively large for small displacements. Furthermore, since the in-plane movement is uniform for the whole region of observation, the resulting rigid body motion can be compensated readily and the error is almost independent of the given displacement. However, for an arbitrary distribution of in-plane displacement, an average in-plane displacement cannot be used for compensation, and in general the error would increase with displacement [9]. Additionally, the in-plane error should not depend on the projected period if correct color encoding is to be carried out. This is confirmed by noticing the similarity of all curves in Fig. 3.6(b) which include also the reference result (labeled BW). This similarity of the results also implies that the presence of residual fringes in the speckle images does not affect the in-plane measurements obtained by the proposed method.

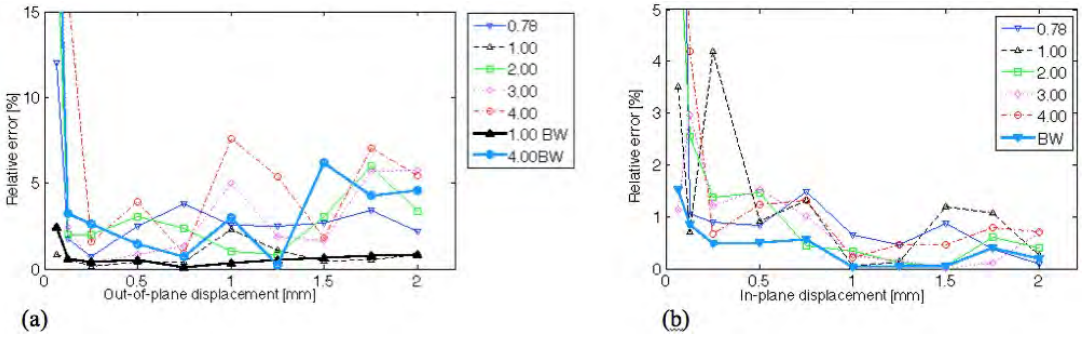

Fig. 3.6. Relative error for measured displacements, (a) out-of-plane, and (b) in-plane, for various projected grating periods (in mm), T. The size of subimages is 64x64 pix. For displaying purposes, the graphs are clipped at 15% and 5%, respectively. The thicker curves correspond to results obtained by standard methods of FP and DIC.

As results in Fig. 3.6 suggest, the average error for the present method is around 1% when projected periods of 1.0 mm are employed. When comparing this value with those obtained in References 7 and 8, which are within 2 and 5%, we can say that the present method shows a good performance. This holds even for uniformly colored objects, such as the one shown in Fig. 3.3, where the resulting errors were similar to the ones presented in Fig. 3.6.

In the case of out-of-plane measurements (no in-plane displacement), if the corresponding speckle images are processed by DIC, then we obtain a radial-like vector field caused by the angular field of view of the object, as shown in Fig. 3.7(a). In this figure, for the case of an out-of-plane movement of 1.5 mm, a maximum in-plane displacement of 0.26 mm is found. This value agrees with that found by using the parameters of the setup (object-to-imaging lens distance of 885 mm and observation size of 250 mm). For three-dimensional displacements, the added non-uniform in-plane displacement arising from the out-of-plane displacement will increase the in-plane error. This, however, can be prevented by the use of a telecentric imaging lens [7] or may be numerically compensated [10].

Similarly, for in-plane measurements, by processing the corresponding fringe images via correlation, we find that the average absolute residual displacement is close to zero, see Fig. 3.7(b). This implies one thing: the speckle information does not appear on the image of fringes; thus, this warranties a considerable reduction of the levels of noise in out-of-plane displacement measurements. Hence, as commented above, it makes unnecessary the application of any directional low-pass filter to the images of fringes.

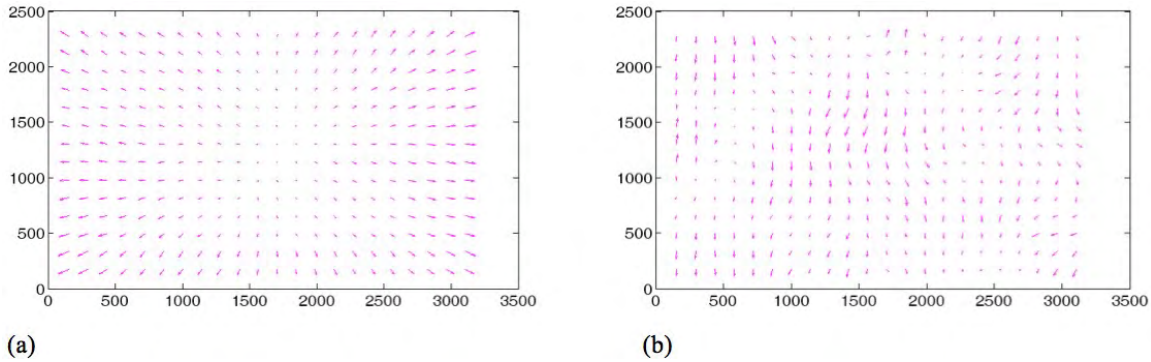

Fig. 3.7. In-plane residual error. (a) In obtaining this vector field, the signal on the blue channel (speckle image) is used. The aluminum plate undergoes an out-of-plane displacement of 1.5 mm. The maximum residual in-plane displacement is 0.26 mm, and is located at the corners. (b) To obtain this graph, the signal on the red channel (image of fringes) is used. An in-plane

displacement of 1.5 mm is given to the plate. The absolute residual average in-plane displacement is 19.5 μm. Dimensions of coordinate axes are pixels.

3.4 Conclusions

In this chapter we presented a color-encoded method that permits the measurement of 3D deformation for opaque objects by a combination of fringe projection and digital image correlation. To achieve this, we used an illuminating image that consisted of a pattern of cyan stripes embedded in a white background. For white-sprayed objects the signal information for DIC was encoded on the blue channel of a recorded image and that for FP on the red channel. To show the feasibility of the technique, a series of measurements was conducted and the error was computed. We found that the overall performance of DIC was better than that for FP with the reported conditions. Furthermore, it was shown that as the content of the DIC signal (speckles) in the resulting images of fringes is quite low, a high level of accuracy of 3D displacement measurements could be reached.

Having all the information required for 3D deformation calculation in one image allows us to carry out analyses of relatively fast events.

3.5 References

1. D. Caspi, N. Kiryati, and J. Shamir, ‘‘Range imaging with adaptive color structured light,’’ IEEE Trans. Pattern Anal. Mach. Intell. **20(**5**)**, 470–480 **(**1998**)**.
2. P. Siegmann, V. Alvarez-Fernandez, F. Diaz Garrido, and A. E. Patterson, “A simultaneous in- and out-of-plane displacement measurement method,” Opt. Lett. **36**(1), 10–12 (2011).
3. L. Fu, Z. Li, L. Yang, Q. Yang, and A. He “New phase measurement profilometry by grating projection,” Opt. Eng. **45**(7), 073601-4 (2006).
4. S. Zhang, “Recent progresses on real-time 3D shape measurement using digital fringe projection techniques,” Opt. Lasers Eng. **48**, 149-158 (2010).
5. S. Rosendahl, E. Hallstig, P. Gren, and M. Sjodahl, “Phase errors due to speckles in laser fringe projection,” App. Opt. 49(11), 2047-2053 (2010).
6. K. J. Gasvik, *Optical Metrology*, (3rd Ed. John Wiley and Sons, Sussex 2003).
7. C. J. Tay, C. Quan, T. Wu, and Y. H. Huang, “Integrated method for 3-D rigid-body displacement measurement using fringe projection,” Opt. Eng. **43**(5), 1152-1159 (2004).
8. P. Siegmann, V. Alvarez-Fernandez, F. Diaz-Garrido, and E. A. Patterson, “A simultaneous in- and out-of-plane displacement measurement method,” Opt. Lett. **36**(1), 10-12 (2011).
9. J. Westerweel, “Fundamentals of digital particle image velocimetry,” Meas. Sci. Technol. **8**, 1379-1392 (1997).
10. L. F. Sesé, P. Siegmann, F. A. Diaz, and E. A. Patterson, “Simultaneous in-and-out-of-plane displacement measurement using fringe projection and digital image correlation,” Opt. Lasers Eng. **52**, 66–74 (2014).

4 Optimization of FP-DIC for multi-colored objects

As noted in Section 3.3, one drawback of FP-DIC is that the in-plane component of displacement is influenced by the out-of-plane component [1]. For the color encoding technique, this issue is shown to be corrected by applying a transformation equation to the imaging lens which is coupled to the camera [2]. Another limitation is that color-encoded signals can only be optimally retrieved as long as the color of the object is neutral.

The aim of this chapter is to extend the analysis of FP-DIC to non-neutral colored objects. We show that for multi-colored objects, by introducing a variation in the setup, results with relatively high-accuracy can be obtained. The variation consists in using two separated light sources for each technique. Then, the optimal design of the setup is obtained by considering coupling effects between the color channels of the camera and of the different light sources. In this analysis, proper selection of the light sources is done by evaluating the contrast of resulting images when examining a plane object.

This chapter is organized as follows. In Section 4.1 we introduce the mathematical model that represents the imaging of a neutral-colored object. In Section 4.2, a description of the spectral characterization of the components of the setup is outlined. Next, in Section 4.3, two formulas for the computation are given, one for FP and the other for DIC. An analysis of contrast is presented in Section 4.4; in this section, the optimal components of the light source are found, for neutral and multi-colored objects. In Section 4.5, we include a displacement analysis that allows us to evaluate the performance of various types of combinations of light sources, when dealing with multi-colored scenes. Then, in Section 4.6, performance of the resulting optical system is evaluated by comparing prescribed and corresponding measured displacements, for multi-colored objects. Finally, our conclusions are given in Section 4.7.

4.1 Imaging of colored objects

The modeling of the imaging process considers a standard FP-DIC setup, as that depicted in Fig. 4.1. The setup consists of an illuminating source (a digital projector or a laser), a camera, an imaging lens, and the object under test. The schematic

diagram also includes a second light source (DIC projector), which can be used in case that the light sources for FP and DIC are spatially separated. As mentioned previously, for DIC, to discard any intrusive effect that originates from surface preparations, the object is illuminated uniformly so that DIC images are formed by the natural texture of the object surface. In this case, however, for objects with relatively smooth surfaces, contrast of the images may become too low. To overcome this situation and, in general, to increase the contrast of images, a separate light source for DIC is proposed. As described in Section 4.4, a separate DIC light source will also enable us to analyze objects with both multicolor content and large dynamic range.

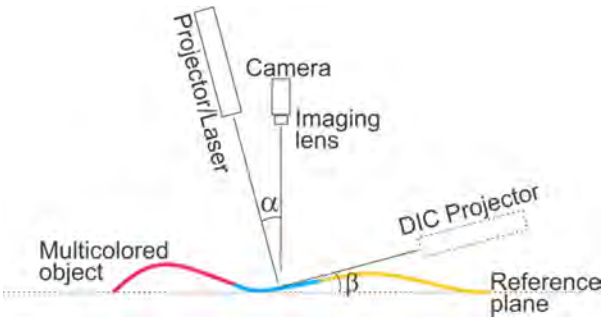

Fig. 4.1. Optical layout for FP-DIC technique.

In order to gain insight of the registering process of non-neutral colored objects, we need to contemplate the spectral characteristics of the setup components: spectral response of the camera, spectral content of the light source [$I(x,y,\lambda)$], and spectral reflectance of the object surface, $O(x,y,\lambda)$, where (x,y) designates a particular position and λ is light wavelength. For a color camera that incorporates a Bayer filter array, the spectral transmittance functions of the red, green and blue filters can be denoted by $r_C(\lambda)$, $g_C(\lambda)$ and $b_C(\lambda)$, respectively. Notice that these functions do not depend on position. Figure 4.2(a) depicts these three functions for the camera used in the experimental work. Also in Figs. 4.2(b)-4.2(d), we present the spectral reflectance of various objects (pigments) and the spectral power distribution of several illumination sources; these figures are fully described in Section 4.2.

Considering the components of the setup, output of the camera, for each color channel [R G B], can be described by [3]

$$\begin{bmatrix} R(x,y) \\ G(x,y) \\ B(x,y) \end{bmatrix} = \begin{bmatrix} \int_0^\infty r_C(\lambda) O(x,y,\lambda) I(x,y,\lambda) d\lambda \\ \int_0^\infty g_C(\lambda) O(x,y,\lambda) I(x,y,\lambda) d\lambda \\ \int_0^\infty b_C(\lambda) O(x,y,\lambda) I(x,y,\lambda) d\lambda \end{bmatrix}. \quad (4.1)$$

When the illumination source corresponds to a digital projector, the spectral power distribution $I(x,y,\lambda)$ can be set by the actual RGB triplet values fed to the projector $[r_P \ g_P \ b_P]$, which in turn depend nonlinearly on the RGB values instructed to the graphics card [3], $[r_{ins} \ g_{ins} \ b_{ins}]$–in Fig. 4.2(f), the nonlinear behavior of the projector employed in this analysis is presented–. Therefore,

$$I(x,y,\lambda) = r_P(x,y) I_{PR}(\lambda) + g_P(x,y) I_{PG}(\lambda) + b_P(x,y) I_{PB}(\lambda), \quad (4.2)$$

where $I_{Pn}(\lambda)$ is the spectral distribution of each illuminating primary color of the projector, with $n = \{R,G,B\}$. By substituting Eq. (4.2) into Eq. (4.1), the composite signal from the camera is

$$\begin{bmatrix} R \\ G \\ B \end{bmatrix} = \begin{bmatrix} \int_0^\infty r_C O I_{PR} d\lambda & \int_0^\infty r_C O I_{PG} d\lambda & \int_0^\infty r_C O I_{PB} d\lambda \\ \int_0^\infty g_C O I_{PR} d\lambda & \int_0^\infty g_C O I_{PG} d\lambda & \int_0^\infty g_C O I_{PB} d\lambda \\ \int_0^\infty b_C O I_{PR} d\lambda & \int_0^\infty b_C O I_{PG} d\lambda & \int_0^\infty b_C O I_{PB} d\lambda \end{bmatrix} \begin{bmatrix} r_P \\ g_P \\ b_P \end{bmatrix}, \quad (4.3)$$

where, for brevity, coordinates (x,y) and (λ) have been omitted.

The off-diagonal elements of this matrix correspond to coupling effects between color channels of the camera sensor. Equation (4.3) can be equivalently indicated by a crosstalk matrix, [3-5]

$$\begin{bmatrix} R \\ G \\ B \end{bmatrix} = \begin{bmatrix} a_{rR} & a_{rG} & a_{rB} \\ a_{gR} & a_{gG} & a_{gB} \\ a_{bR} & a_{bG} & a_{bB} \end{bmatrix} \begin{bmatrix} r_P \\ g_P \\ b_P \end{bmatrix}, \quad (4.4)$$

where the first subindex of matrix coefficients a_{mn}, $m = \{r,g,b\}$, designates color channel of the camera.

To disregard the influence of the object in Eq. (4.4) and consider only the coupling effects of the combination camera-projector, a white object can be considered (or even better, direct illumination of the camera sensor by the projector may be

assumed), where $O(\lambda) = c_0$, with c_0 being a constant. In this case, matrix coefficients can be measured by illuminating the object consecutively by pure red, green and blue, and separating the registered images into each color channel [4-6]. Matrix coefficients can then be computed by evaluating either the modulation amplitude, for the case of fringe pattern projection, or the average intensity, for the case of uniform illumination.

As noticed in [5], one useful feature of Eq. (4.4) is that it allows us to recover the instructed image from the corresponding registered image, via inversion of the crosstalk matrix. This implies that any coupling effect can be effectively reduced. In this work, the crosstalk matrix helps us select the color channels of the camera that will register the FP and DIC signals. In some tests, the crosstalk effect is to be reduced (for neutral-colored objects, Section 4.4.1), but in others, enhanced (for multi-colored objects, Section 4.4.2).

4.2 Spectral characterization

Spectral specifications related to the components of the experimental optical setup are presented in Fig. 4.2. Figure 4.2(a) shows the spectral response of the camera sensor (Lumenera Lt225c, 1088x2048 pix, 18-55 mm Nikon lens) [7], for each of the RGB primary colors (abbreviations are defined in figure title). We can notice the ability of the sensor to detect near IR and UV. Overlapping between neighbor and non-neighbor channels can be noted as well. Two additional vertical lines are incorporated in this figure to indicate location of the emitting spectrum of a sodium lamp (emitting peak at 589 nm, Pasco OS-9287B) and UV LEDs (peak at 394 nm, bandwidth of 7 nm).

Figure 4.2(b) depicts the spectral reflectance curves of the color-saturated pigments used in this work. Reflectance measurements were done by a PerkinElmer spectrometer, Lambda 900. These particular pigments are commonly used in the local leather footwear industry, and therefore they show highly saturated colors. We selected various representative pigment colors: red, green, blue, yellow, black, white, gray and gold; gray and gold are slightly darker variations of white and yellow, respectively. From plots in Fig. 4.2, we can see that all pigments present significant reflectance values close to UV and around 850 nm. By considering the vertical lines that specify the location of the UV and sodium light sources, we can note that UV

is reflected almost equally by all pigments (except for the white and gray pigment). The same result holds for the sodium light source, but only for red, green, blue, and black pigments. The fact that the reflectance does not depend on object color, suggests the possibility to analyze either multi-colored objects or scenes with high-dynamic range.

Also observed from Fig. 4.2(b), it is the high values of reflectance in the IR, with the red and yellow pigments standing out.

In Fig. 4.2(c), spectral distributions of light sources, for FP, are presented. These curves were obtained by an Ocean Optics spectrometer, USB2000. Two FP light sources are used: a blue laser (OxLasers, OX-BX8 Pro, 4 W, emitting at 447 nm), denoted by *lasB*, and a digital projector –Epson EH-TW-6100, 1080x1920 pix, 2300 lm–. Spectral compositions of the pure colors produced by the projector are included, and are indicated by "*p*" –all of them show a broad spectral width–. Analogously, Fig. 4.2(d) contains the spectral distributions of the light sources for DIC. In this case, five distinct sources are analyzed: one matrix of 4x10 5-W IR LEDs –center wavelength at 850 nm–, (*ledIR*); a matrix of 20x20 1-W red LEDs –at 640 nm– (*ledR*); a matrix of 4x10 3-W UV LEDs –at 394 nm– (*UV*); a DIC projector that produces uniform illumination –Epson PowerLite, 800x1280 pix, 3000 lm–; and a sodium lamp (*Na*). For the DIC projector, only the CMY colors are used. As shown, spectral distributions of the two projectors are different. Besides, their spectral distributions reveal the presence of weak crosstalk.

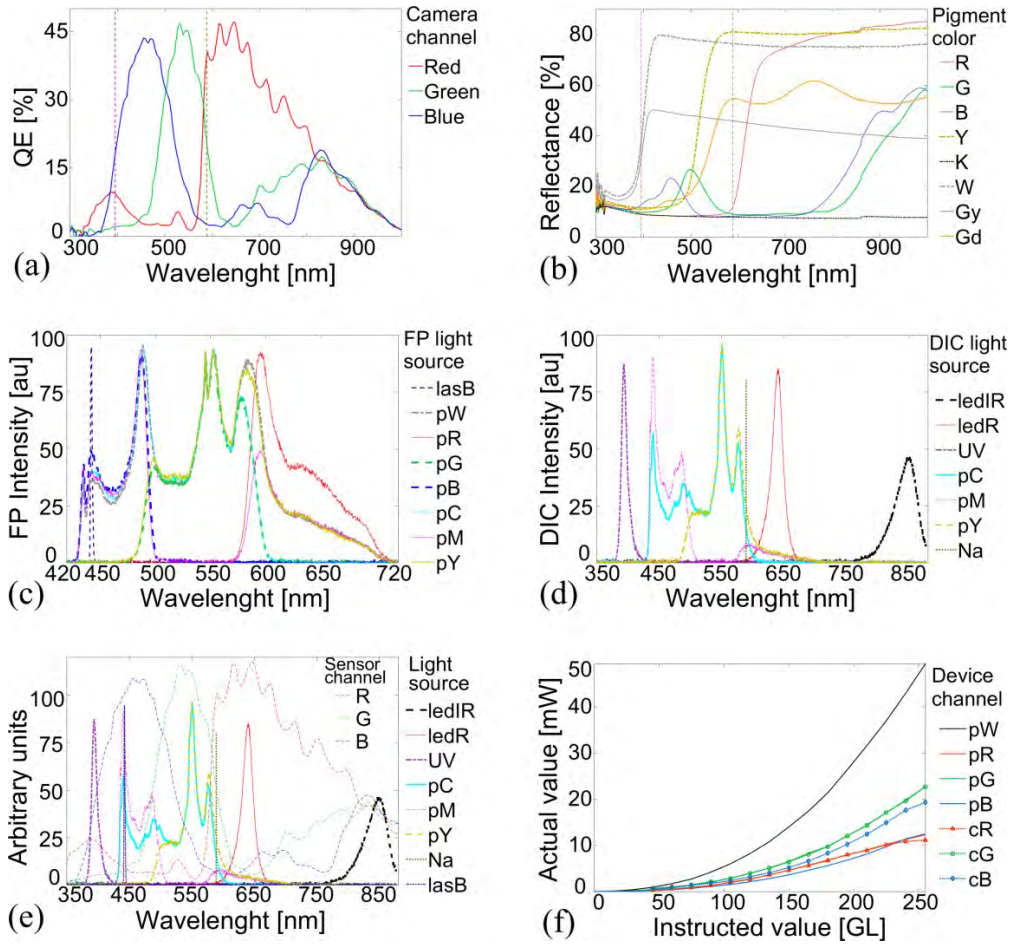

Fig. 4.2. (a) Spectral response –quantum efficiency, QE– of each RGB color channel of camera sensor; (b) spectral reflectance of various pigments (primary RGB colors, yellow *Y*, black *K*, white *W*, gray *Gy*, and gold *Gd*); (c) spectral distribution of FP light sources (in legend, words starting with "p" stand for projector, and the second letter indicates primary RGB color or secondary CMY color; also *lasB* designates the blue laser); (d) spectral distribution of DIC light sources (*led* denotes a matrix of LEDs; *R* for red and *IR* for infrared; *UV* stands for ultraviolet LEDs matrix; and *Na* is sodium lamp); (e) Superposition of Figs. 4.2(a) and 4.2(d); (f) nonlinear behavior of FP projector (solid lines) and of projector-camera combination (dotted lines with markers); c designates camera. *GL* and *au* correspond to gray levels and arbitrary units, respectively.

For visualization purposes, in Fig. 4.2(e) we present the superposition of the spectral compositions of the camera sensor, DIC light sources, and blue laser. Some facts are worth to highlight: (1) IR from LED matrix is detected almost equally by all camera channels; (2) both UV from LEDs and light from blue laser are strongly detected by the blue channel, but weakly registered by the green channel; in this case, response of the red channel is larger than that of the green channel; (3) red LED illumination is selectively detected by the red channel; (4) red spectral

distribution is strongly reflected by W, Gy, Gd and R pigments, but weakly by G and B pigments.

In general, response of the camera to the colors of the projectors is defined by the crosstalk matrix, as is derived below.

As shown in Section 4.4, in selecting the optimum color from the FP projector, values of the individual electronic gains of the camera channels have to be adjusted. This is to partially compensate for the nonlinear response of both projector and camera. In the case of a projector, actual generated light intensity and RGB triplet values instructed to the graphics card show a nonlinear relationship. In Fig. 4.2(f) we present the nonlinear behavior of the projector, indicated by solid curves. The actual values of intensity are measured by a Newport power meter –M-815– located at the exit of the projector. In the case of white light, the RGB triplet is set to (255,255,255). As noticed, white color intensity is approximately equal to the sum of the pure primary colors. Moreover, note the imbalance between primary colors, with green being clearly favored when compared to red and blue.

Now, to understand the effect of the camera on the projector throughput, a white object is illuminated by FP projector (projecting each primary color one at a time) and the reflected signal is detected by the camera. Similarly to the situation of reinforcement of green by the projector, the camera reinforces notably the signal from blue channel, as shown by the curves indicated by dotted lines with markers, Fig. 4.2(f) –corresponding gray level values produced by camera software are scaled to mW, in such a way that the maxima for greens coincide–. From the two sets of curves, solid and dotted, we observe that curves for red and green tightly coincide, and therefore the camera response to red and green is approximately flat throughout the dynamic range. To conclude the latter, we have to consider that the measured response of the camera encompasses nonlinearities of both camera and projector. As shown below, the theoretical crosstalk matrix of the camera-projector combination yields ($a_{rR}=0.54$, $a_{gG}=1.00$, $a_{bB}=0.54$). When comparing these values with the normalized RGB values given by dotted curves of Fig. 4.2(f), at gray level of 255, ($a_{rR}=0.51$, $a_{gG}=1.00$, $a_{bB}=0.85$), we note clearly the difference related to the blue response, which should stem from the approach adopted by the camera software to process the RGB signal.

The theoretical crosstalk matrix of the projector-camera combination can be obtained by considering the spectral distributions of the RGB outputs from FP projector, Fig.

4.2(c), and the spectral response of camera sensor, Fig. 4.2(a), via Eq. (4.3): $(0.54\ \ 0.34\ \ 0.03;\ 0.11\ \ 1.00\ \ 0.18;\ 0.03\ \ 0.32\ \ 0.54)$–object spectral reflectance $O(x,y,\lambda)$is set to 1–. From this theoretical matrix, we can notice that signal from green channel of the projector is strongly coupled onto both red and blue channels of the sensor, with values of 0.34 and 0.32, respectively (couplings are scaled within the range 0-1). Smaller couplings are regarded to the green channel of the sensor, when projecting red and blue colors (0.11 and 0.18, respectively). Also, overlapping between red and blue is relatively weak (0.03). Additionally, differences in the values of the diagonal account for the imbalance between the three primary colors (0.54, 1.00, and 0.54), which apparently are similar to the values given by the normalized nonlinear relationship of the projector, at gray level of 255, (0.50, 1.00, and 0.55), which are derived from the plots indicated by solid lines in Fig. 4.2(f).

Values of the latter theoretical coupling matrix are verified experimentally. Firstly, gains of the camera channels are set to 1 (no-gain condition), and then the camera registers a uniform light field coming directly from FP projector (no object is used), where each primary color is projected sequentially; instructed values are indicated by triplets; for example, for pure red, (255,0,0). The resulting matrix is $(0.49\ \ 0.00\ \ 0.00;\ 0.04\ \ 1.00\ \ 0.12;\ 0.00\ \ 0.00\ \ 0.84)$, which is represented graphically by the group of the three leftmost bars in Fig. 3(a), case 1.0r (the first bar is formed by 0.49, 0.04 and 0, in a normalized mode; i.e., this bar refers to the recorded RGB signals when red is projected). We can observe that the coupling values are similar to those obtained theoretically, except for the second bar, where it is seen that red and blue crosstalk signals become practically null.

As gains of the camera channels are varied –minimum and maximum gains of camera are 1 and 4, respectively–, the crosstalk matrix of FP projector is modified. This behavior is presented in Fig. 4.3(a). In this figure, each bar represents one column of the corresponding coupling matrix and the length of each RGB color segment designates the coupling value to the corresponding RGB channel –labels located exactly below the bars, {R, G, B}, denote the illuminating primary color–. For visualization purposes, lengths of all bars are set to 1; then, these types of plots indicate the relative response of each color channel to the corresponding illuminating color produced by the projector. Further, the bottommost horizontal labels designate both the value of the gain of camera channel and the corresponding boosted

channel; e.g., 2.5r implies that the gain of red channel is 2.5, and that of the others, green and blue, are 1.0.

Considering the three first groups of bars in Fig. 4.3(a), it is observed that when the gain of the red channel is changed from 1.0 to 2.5 and 4.0 (while other gains are set to 1.0), the red signals detected by all camera channels increase, while green and blue signals decrease. Accordingly, the crosstalk matrix is changed and therefore the matrix depends on the camera gains. A similar result is obtained when gain of the other channels is increased. However, for the case when green gain is augmented, the effect is more marked.

It is worth pointing out that crosstalk values obtained by direct projection of light onto the camera are almost identical to those measured by using an intermediate white object, as done in [4]. Further, when the illuminating uniform field is replaced by a pattern of fringes, only slight differences are noticed as well. In all analyses presented in this work it is assumed that all channel gains of the projectors are set to 1.0.

In Fig. 4.3(b) we include a similar analysis to that done for FP projector, but for DIC sources (UV and IR) and blue laser –denoted by U, I and L, respectively–. However, in this case a complete crosstalk matrix cannot be formed for each light source, but only one column. Then, a bar corresponds to the RGB signals registered by the camera when a particular light source is used. Considering the case of all gains set to 1.0 –denoted by 1.0r–, we note that both UV and blue laser are mostly detected by blue channel, and that IR is coupled almost equally onto all channels. Besides, for UV case, there is a non-negligible coupling onto both red and green channels. Additionally, as gain of only one camera channel is increased, a similar behavior as that found for FP is obtained; that is, the signal of the reinforced color channel increases at the expense of the signals of the other camera channels.

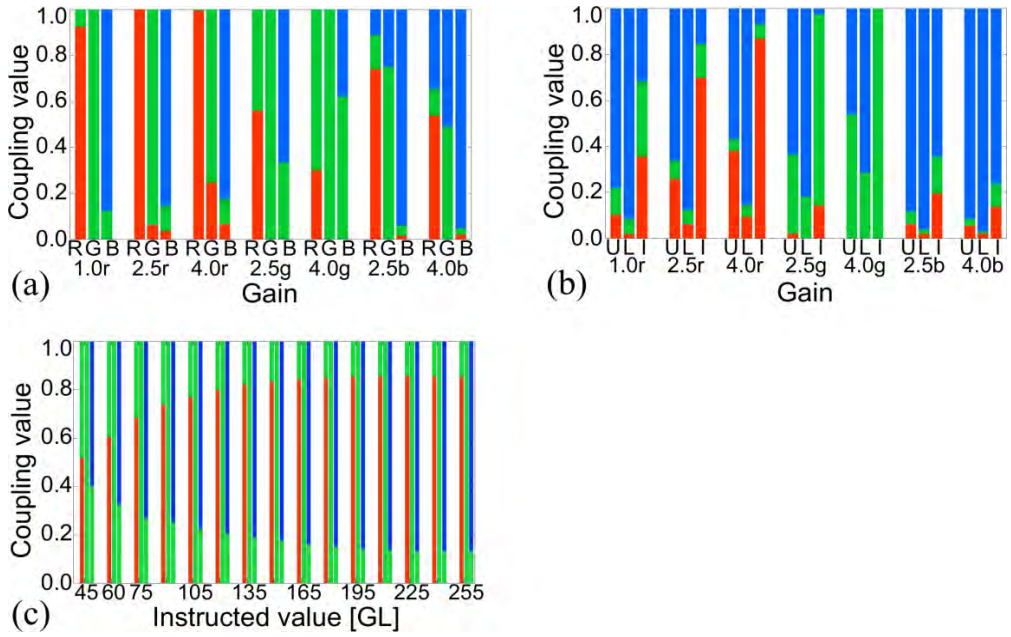

Fig. 4.3. Relative coupling values. For (a) FP projector; (b) UV (U), blue laser (L), IR (I); (c) Dependence of coupling on instructed RGB value to FP projector.

Apart from channel gains of the camera, another parameter that influences the coupling matrix is the intensity of the illuminating beam. In particular, for the FP projector, the intensity of the illuminating beam is directly related to the instructed RGB values. Regarding this case, the crosstalk matrix is measured as the intensity of each projector channel is varied from 0 to 255; resulting matrices are exhibited in Fig. 4.3(c) –all channel gains of camera are set to 1–. Each group of 3 bars correspond, going from left to right, to red, green, and blue illumination, respectively. Each group is associated with a particular gray level; for example, abscissa value of 45 implies illumination triplets (45,0,0), (0,45,0) and (0,0,45). Notice that no evaluation is done for gray values smaller than 30, since in these circumstances, noise level is on the order of the signal. Information given by Fig. 4.3(c) is the same as that shown in Fig. 4.2(f), denoted by dotted lines (with markers), but normalized. One advantage of Fig. 4.3(c) is the straightforward visualization of how the fractional composition of the camera RGB signals varies with intensity; for instance, as gray level is diminished, green signal increases, in detriment of red and blue signals.

4.3 Contrast definitions

Since accuracy of displacement measurements is largely dependent on the contrast of the registered images, we will use this parameter to estimate the performance of the employed light sources. Considering that the nature of the spatial structures for FP and DIC images is different, two expressions for contrast are defined.

For FP, we define the following expression for fringe contrast,

$$C_{FP} = \langle b(x,y)/a(x,y)\rangle \left(w_{F,MIN}/w_F\right)\left(K_{MIN}/K\right)^{1/3}, \qquad (4.5)$$

where angular brackets denote the operation of ensemble spatial averaging. The first factor of Eq. (4.5), $\langle b(x,y)/a(x,y)\rangle$, refers to the common definition of contrast, which incorporates the parameters appearing in Eq. (2,2), i.e., the modulation amplitude and the background level [8]. These two parameters can be obtained by filtering the Fourier spectrum of the corresponding image $I(x,y)$, and transforming back to the spatial coordinates: $a(x,y) = \left|\Im^{-1}\left\{\tilde{I}(f_x,f_y)H(f_x,f_y)\right\}\right|$ and $b(x,y) = 2\left|\Im^{-1}\left\{\tilde{I}(f_x,f_y)H(f_x-f_0,f_y)\right\}\right|$, $\tilde{I}(f_x,f_y) = \Im\{I(x,y)\}$ and $H(f_x,f_y)$ is a band-pass filter applied to image spectrum.

Contrast of FP images is reduced by the presence of any residual speckle noise (arising mainly from the DIC signal). We found that the larger the noise content, the wider the spectral side lobes. Thus, an additional multiplicative parameter is included in Eq. (4.5), $w_{F,MIN}/w_F$, where w is the width of the first spectral lobe for any image, at 85% of the maximum level (at this percentage value, the shape of the spectral lobe is smooth and identification of the corresponding pixel is straightforward), and $w_{F,MIN}$ is the value of w, a minimum, that corresponds to the image with maximum contrast. The third factor in Eq. (4.5), $\left(K_{MIN}/K\right)^{1/3}$, is included to further enhance FP contrast differences between images; this factor weighs the level of scattering of intensity values with respect to the mean, where K is the number of points that fulfill the condition $\left|\left(I(x,y)-\langle I(x,y)\rangle\right)/\langle I(x,y)\rangle\right| < 0.1$; then, K_{MIN} corresponds to the image with the highest contrast. In the latter condition, a relatively small value of the threshold, 0.1, is used since intensity values of low-contrast images are generally concentrated within a narrow range of values.

For DIC, we define contrast as

$$C_{DIC} = \left\langle \frac{\sigma_{local}}{\langle I_{local} \rangle} \right\rangle \sqrt{\Gamma_{MAX} / \Gamma} \left(K_{MIN} / K \right), \qquad (4.6)$$

where subindex *local* makes reference to a subset of data (subimages of 7x7 pix) and σ_{local} is the respective standard deviation. The first factor in Eq. (4.6) refers to the expression generally used in laser speckle fields [9]. Analogously to the case of FP contrast, to boost contrast differences, two more factors are added. One of the additional factors considers the effect of any residual fringes and the other follows the same reasoning as in FP (notice a difference in the exponent of the last factor, which reflects the fact that spatial features of fringes and speckle are different). The first additional factor is $\sqrt{\Gamma_{MAX} / \Gamma}$, where Γ is the value of the maximum amplitude of the first side lobe, in frequency domain; hence, Γ_{MAX} represents Γ for the image with the maximum contrast.

Contrast values for FP and DIC are scaled in such a way that they take values in the range 0-100. There is no relationship between both scales.

4.4 Contrast analysis

4.4.1 Neutral-colored objects

As mentioned in Sec. 4.3, contrast is taken as the evaluation criterion for proper selection of light sources, for FP and DIC, when these techniques are used simultaneously. Therefore, all possible combinations of FP and DIC light sources are tested for representative object colors (pigments); the object under analysis is a diffuse reflecting flat surface formed by a layer of pigment (thickness, 5 mm, and rms roughness of 0.7 mm). The DIC light beam presents constant intensity and the FP beam is formed by a pattern of fringes.

Several configurations for the illumination sources are tested (to name them, the first component of the name corresponds to the device generating the DIC signal and the second one, to the generator of the FP signal):

(1) Just one projector [denoted by *(1p)*; here, both signals for DIC and FP are produced by only one projector], e.g. W-C(1p), meaning cyan fringes embedded in white background,

(2) Two projectors, *(2p)*, e.g. C-R(2p), implying projection of a cyan uniform beam generated by DIC projector and red fringes by FP projector (half a fringe period is black),

(3) Projector-blue laser, *p-lasB*, e.g. pY-lasB –yellow background produced by DIC projector and fringes by blue laser–,

(4) Matrix of IR LEDs-blue laser, *IR-lasB*,

(5) Matrix of IR LEDs-projector, *IR-p*,

(6) Matrix of red LEDs-blue laser, *ledR-lasB*,

(7) Matrix of red LEDs-projector, *ledR-p*,

(8) Matrix of UV LEDs-blue laser, *UV-lasB*,

(9) Matrix of UV LEDs-projector, *UV-p*,

(10) Low-pressure sodium lamp-projector, *Na-p* (this configuration is used only for multi-colored objects, Section 4.4.2).

Previous works using configuration (1) have already been reported [2, 10-12]. In configurations (2)-(10), illuminating beams for DIC and FP are produced by separate light sources. Separating the light sources for FP and DIC allows us to widen the possibilities for adapting the illuminating beams to the features of the objects, such as spectral reflectance distribution and level of roughness. In this way, the intensity of the two beams can be adjusted independently of each other; consequently, high-power sources can be incorporated into the setup, enabling imaging of large and even dark objects. Additionally, illumination angle for DIC can be selected as to optimize the contrast of DIC images (any production of shadows can be avoided by use of multiple DIC sources that can be positioned as to achieve both different illumination angles and different directions of illumination).

For FP and DIC, images of size 731x2048 pix are employed, which corresponds to 10.6x29.8 cm^2. Angles of illumination α and β, for FP and DIC, respectively, are 9.3° and 30° (see Fig. 4.1). To promote the white-speckle effect of DIC images and hence their contrast, β is set to relatively low values.

Considering FP and DIC, distances from illumination source to object are 83.5 cm and 55 cm, respectively (object-to-camera distance is 66.9 cm). In FP, a

projected period of 2 mm (duty cycle of 50%) is used [11] (generated by either the FP projector or the blue laser); when the projected grating is generated by the blue laser, a combination of a Ronchi ruling of 1000 lines/in and a 20-X microscope objective are used (distance between ruling and objective is 21.5 mm).

In Fig. 4.4, we include exemplary zoomed-in images (58x87 pix) obtained at each stage of the procedure for calculating contrast. Each object color is represented by one row of images, where we include, first, going from left to right, the captured image with white illumination (designated as the real image); then, the image recorded with the optimal combination of light sources, considering only FP contrast; and finally, the separated images associated with camera color channels. As verified by quantitative results in Fig. 4.5(a), the best combination of light sources for maximum FP contrast is the combination including a uniform beam produced by the red LEDs (DIC light source), and blue fringes by FP projector (combination ledR-pB) –this is an expected result since red and blue channels present the lowest crosstalk between them–. Therefore, in all cases presented in Fig. 4.4 [except for case (b)], the light combination corresponds to ledR-pB, and the fringe pattern is extracted from the blue channel and the DIC image from the red channel. In case represented by Fig. 4.4(c), for green pigment, the ledR-pG (red background produced by LED matrix and green fringes by FP projector) gives a slightly larger contrast than ledR-pB (recall that green crosstalk to blue channel is relatively strong).

Gains of camera channels for each case in Fig. 4.4 are as follows; Fig. 4.4(a) [3.2, 1.0, 1.0]; Fig. 4.4(b) [1.0, 1.0, 1.7]; Fig. 4.4(c) [1.2, 1.0, 1.5]; Fig. 4.4(d) [1.2, 1.0, 1.0]; and Fig. 4.4(e) [1.0, 1.0, 1.0], where triplets refer to [R, G, B] –exposure time is 500 ms for all cases–. Notice that gain of red channel is generally large, which compensates for the reduction of the red signal done by the projector, as pointed out in Sec. 4.2 –this compensation effect can be seen by comparing cases 1.0r and 2.5r in Fig. 4.3(b)–. From the recorded images, we can observe that all images are notably red. A consequence of the incremented red gain is a reduction of residual fringes in DIC images –to avoid the emergence of residual speckle in FP images, intensity of DIC source should be moderate–.

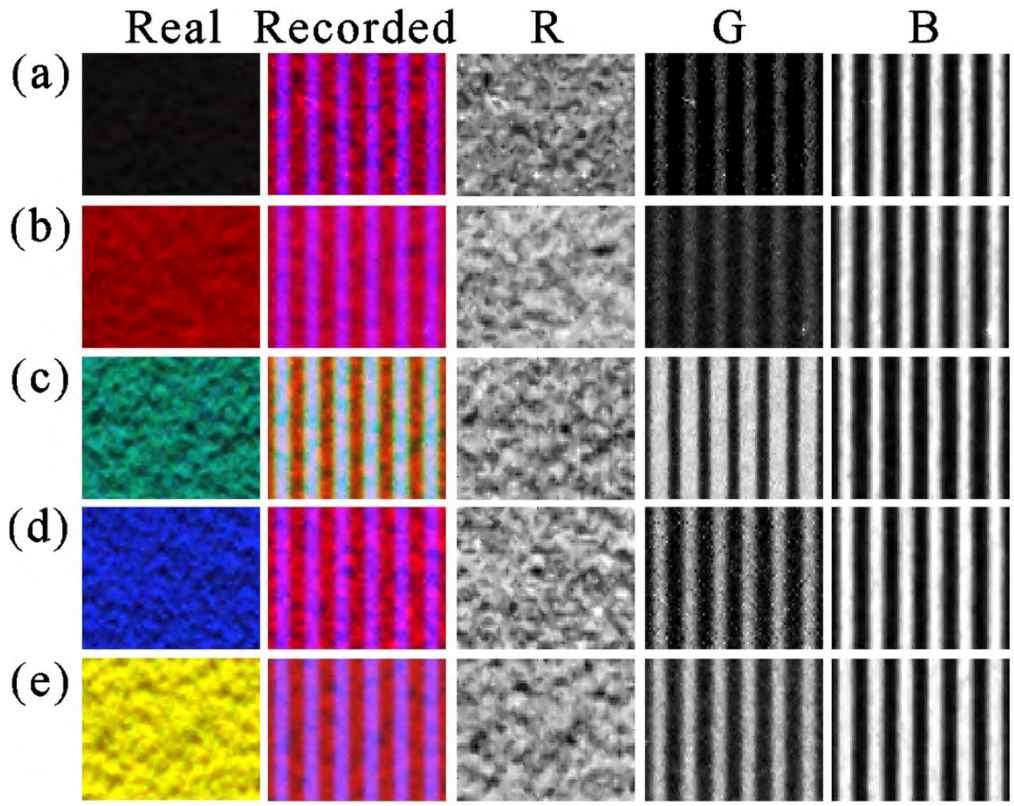

Fig. 4.4. Exemplary zoomed-in processed images for each neutral-colored object (we show only cases of optimal illumination for maximum FP contrast). (a) Black pigment. (b) Red pigment. (c) Green pigment. (d) Blue pigment. (e) Yellow pigment.

Complete quantitative results of contrast are presented in Fig. 4.5, for fringe illumination –FP–, Fig. 4.5(a), and spatially uniform illuminating light –DIC–, Fig. 4.5(b). On obtaining these data, Eqs. (4.5) and (4.6) are used, respectively. Regarding DIC, images are divided in subimages of 15x15 pix (with no overlapping), so reported values correspond to the average of the contrast of the subimages. Numerical values of the contrast in the two plots are unrelated, where their maxima of scale are assigned to be 100.

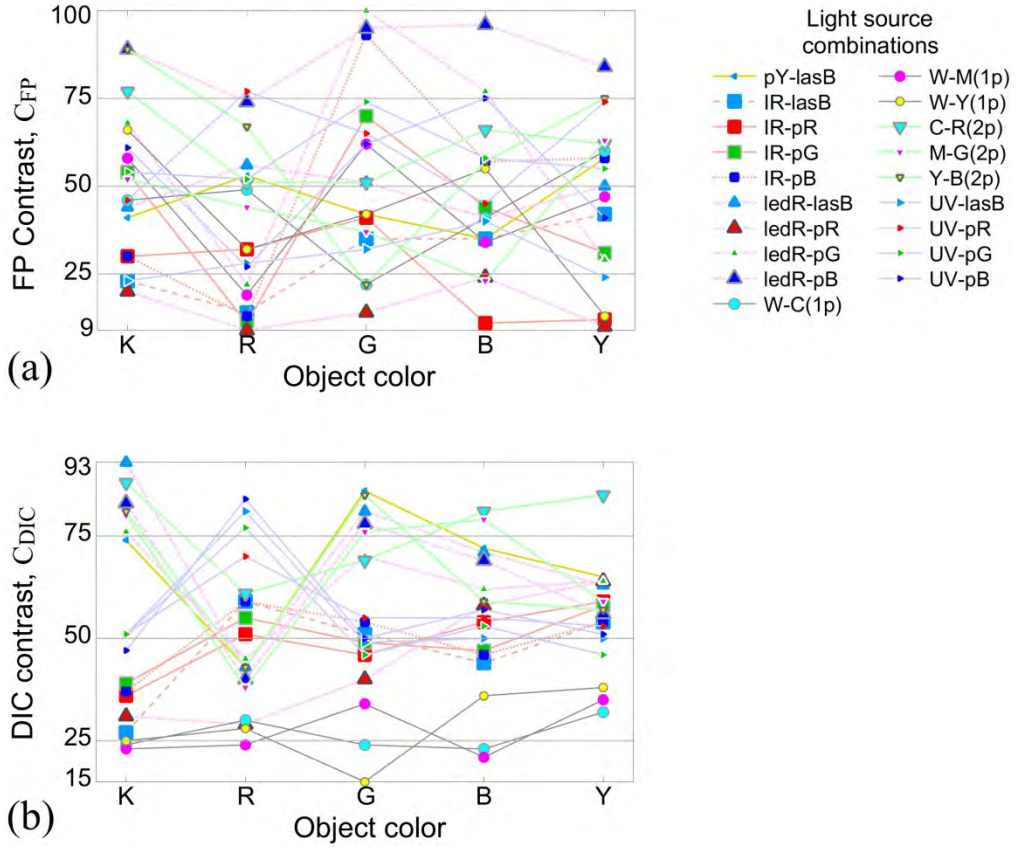

Fig. 4.5. Plots of contrast. (a) FP, (b) DIC. Legend is common to both plots, and notation is as follows: first part of name refers to DIC light source, and last part to FP light source; "p" stands for projector; (1p) means that only one projector (FP projector) is used for both FP and DIC, and (2p) denotes that two different projectors are used (one projector for FP and another for DIC). An instance of light combination is UV-pR, which implies that matrix of UV LEDs is used for DIC and light by red channel of FP projector for FP (red fringes on a black background). More details are given in text.

As observed from Fig. 5(a), considering all pigment colors, the optimal light-source combination for FP is ledR-pB (red LEDs for DIC and blue light from FP projector for FP). Similarly, from Fig. 5(b), the combination that produces the highest DIC contrast is C-R(2p) –cyan from DIC projector and red from FP projector–. Further, considering both techniques, the combination with the highest performance is ledR-pB. In addition to this, one-light-source configurations (shown by black line) present low contrast in DIC; this is mainly because of the limitation of the DIC incidence illumination angle, which is fixed by FP angle. FP angle is generally set to small values to avoid any production of shadows.

In general, to achieve the best performance of any combination of light sources, first, intensity of FP source is maximized (up to a certain gray level from 150-255) to obtain high-contrast fringes and relatively low content of residual speckle in FP image. Gain of FP channel should be small to obtain a low level of background. Then, DIC intensity is added, taking care that no image saturation occurs and that no residual speckle is introduced in FP image. Besides, to reduce the content of residual fringes in DIC image, gain of DIC channel should be relatively large.

4.4.2 Multi-colored objects

In previous works [3, 6], measurement of shape in multi-colored objects has been reported; in those works, color-encoded signals are used, and the main reported limitation is related with the identification of the signals. In the FP/DIC method, the same problem arises when the object contains multiple colors; and evidently, the previous results obtained for neutral objects do not hold. In multi-colored objects, it is common to deal with relatively large dynamic ranges of the scenes, what complicates measurements.

To get insight in the behavior of multi-colored objects, we analyze three different scenes, each with a distinct composition of colors. The three cases are presented in Fig. 4.6, where the first row of images, Fig. 4.6(a), represents an object formed by 5 stripes of different color (from each stripe, a zoomed-in region –58x29 pix– is taken, and these small regions are arranged as shown). Figures follow the same spatial arrangement used in Fig. 4.4. In Figs. 4.6(a) and 4.6(b), only the combination of light sources with the best overall performance (UV-pB) is shown (to evaluate the distinct light combinations, we proceed as in the case of neutral objects, but measuring contrast in each stripe, for each light combination). Figure 4.6(b) refers to an object composed of 6 distinct colors (a stripe with close-to-white pigment is added to the case of 5 colors), and this variation allows us to model a larger dynamic range at UV.

Third row of images, Fig. 4.6(c), displays the case of an object with only 4 colors, but illuminated by Na-pG (in this case, size of subimages is 58x44-pix). In some subimages, a cross is used to indicate that the subimage should not be considered for analysis, since it is not part of the full image. In contrast to this, white

subimages do correspond to recorded full images, and they are associated with fully saturated cases.

Note that signals of FP and DIC are extracted from green and red channels, respectively. Blue channel is not used because it gets saturated readily when analyzing objects with high-dynamic range.

Gain of camera channels and exposure time, for each part of Fig. 4.6 are, Fig. 4.6(a) [2.5, 1.0, 1.0, 60]; Fig. 4.6(b) [1.7, 1.0, 1.0, 20]; and Fig. 4.6(c) [2.4, 1.0, 1.0, 500]; where the elements of the quadruplets refer to the RGB channel gains and exposure time, in ms, respectively. By incrementing the gain of the red channel of the camera, the spatially uniform UV beam is forced to couple into red channel, and this gives rise to the DIC signal [as depicted in Fig. 4.3(b), case 2.5r]. UV intensity value is selected as to avoid a large background in FP image. For scene with 6 colors, not all subimages corresponding to blue channel get saturated, since the overall intensity level is set to a lower value than the 5-color scene (recall that incorporation of the gray pigment causes a larger dynamic range).

In case of sodium lamp illumination, a relatively large exposure time is used. This compensates for the relatively low power of the lamp.

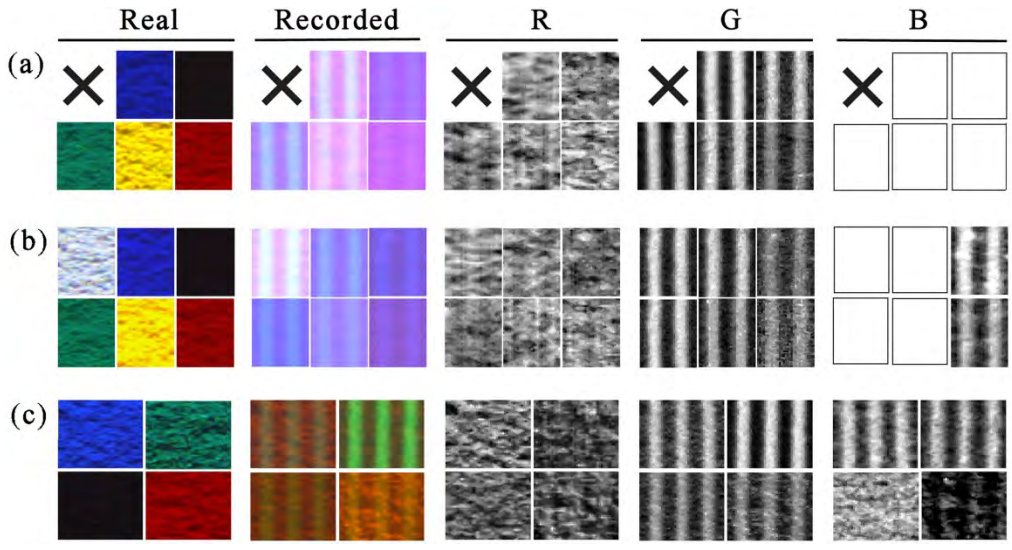

Fig. 4.6. Exemplary zoomed-in processed images for each multi-colored object (we show only cases using optimal illumination). (a) 5-color object. (b) 6-color object. (c) 4-color object.

With regard to multi-colored objects, the most important requirement of an appropriate light combination is that both DIC and FP light beams have to be reflected as uniformly as possible by all stripe colors. Additionally, the camera channel where fringes are to be detected should couple the less to the color used for speckle and vice versa [Figs. 4.2(b), 4.2(c) and 4.2(e) help us visualize these requirements]. Let us analyze, for example, the suitability of IR-pB. From Fig. 4.2(b), we see that reflectance values of black and yellow pigments, at IR (850 nm), are relatively dissimilar; hence the dynamic range of the scene becomes large, and any light combination using IR will not yield acceptable displacement measurements. Besides, as IR is detected by all camera channels, the resulting signal becomes a large background, which in turn decreases the contrast of fringes.

For configurations that use only one projector, difficulties arise from limitations to control independently the intensities for FP and DIC and limitation to adjust the DIC illumination angle. Therefore, one-projector configurations present the lowest performance.

Unlike IR, UV is reflected more uniformly by all pigments, and therefore some combinations incorporating UV, like UV-pB, produce the best results; blue fringes, by crosstalk, are registered on green channel (blue channel gets saturated and is useless) and speckle field is detected on red channel. This can be seen from Fig. 4.3(b), case 2.5r, where UV is strongly detected by red channel (this helps enhancing speckle contrast) and weakly by green channel (causing a low background in FP image).

In all three types of scenes tested, the camera gamma value is adjusted as to increase the signal from low-reflectance stripes (gamma value is 4.0 for the 5- and 6-color scenes and 2.0 for the sodium illumination, where scale of gamma values is 0.1-10, 1.0 representing a linear relationship between input intensity and output gray scale).

4.5 Displacement analysis

Performance of light combinations can be complementarily evaluated by the accuracy of the measurement of three-dimensional displacement. For this aim, measurement of prescribed displacements is done. Instructed displacements are of 1 mm, both in-plane and out-of-plane displacements, and they are produced by a Thorlabs stage,

which shows an accuracy of 1.25 μm. Out-of-plane displacement is obtained by Eq. (2.8), and in-plane, as described in [11], by software proVision-XS PIV, from IDT, where subimages of 24x24 pix are used. Influence of out-of-plane component on in-plane results is compensated as in [12].

In this analysis, images of a scene with different color content are registered, and then each color stripe is separated into its RGB signals. When building up the object under analysis, V-shaped depressions are formed along the boundaries between neighbor stripes. The displacement is calculated for individual color stripes. Figure 4.7 illustrates the results of one of the measurements; in Figs. 4.7(a) and 4.7(c) we show the out-of-plane, OP, and in-plane, IP, components of displacement, and in Figs. 4.7(b) and 4.7(d), their respective cross sections (located at the center of the image, in horizontal direction). In Fig. 4.7, the order of the colors is (from left to right) green, blue, yellow, black and red. As observed, for the out-of-plane results, high levels of noise appear in calculations along the boundaries between neighbor stripes (these regions are not included in calculations). Since the boundaries present random depths on the order of the period of the fringes, they alter locally the period of the fringes; these random alterations are slightly different for the reference and displaced images, and in the end this is reflected as noise in the phase maps.

Further, the largest errors are related to the red stripe, which is due to the low reflectance that this pigment color presents to blue light. Also it is noticed from Fig. 4.7 that in-plane results show smaller variations when compared to the out-of-plane calculations; this is due to the fact that, unlike point-wise calculations for out-of-plane displacement, in-plane calculation involves subwindows with finite size.

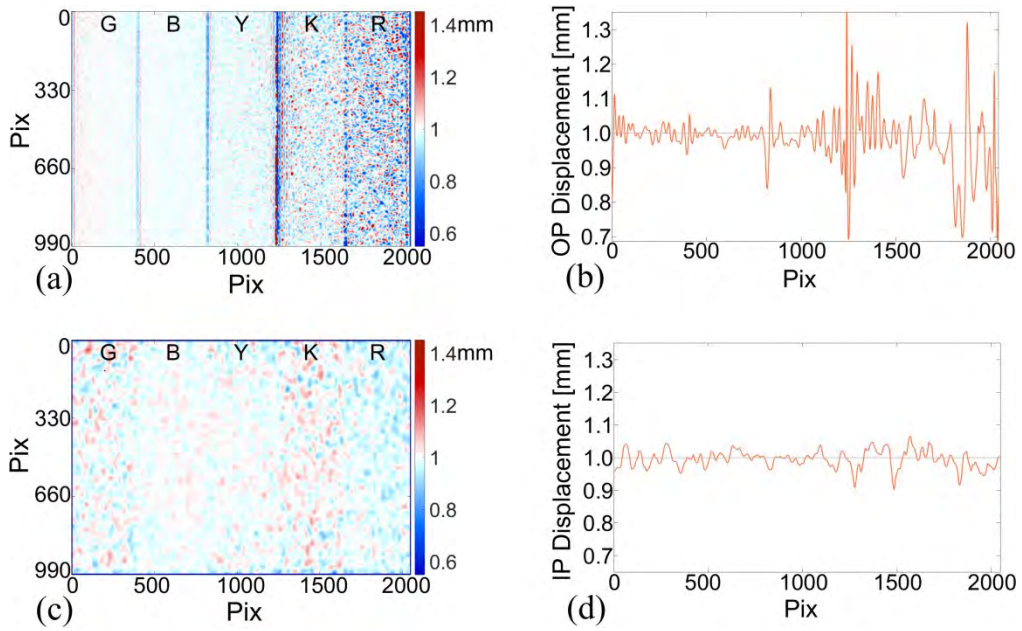

Fig. 4.7. Typical measurement of three-dimensional displacement in multi-colored objects (instructed displacement is 1.0 mm). (a) Out-of-plane component. (b) Horizontal cross-section at center of Fig. 4.7(a). (c) In-plane component. (d) Horizontal cross-section at center of Fig. 4.7(c).

Accuracy is evaluated by computation of the absolute percentage relative error and the standard deviation. Results regarding these parameters are shown in Figs. 4.8(a) and 4.8(b), for FP and DIC, respectively (only 6 light combinations that yield acceptable results are reported). In these figures, stripe color corresponds to x-axis, and relative error to y-axis. Each curve represents a particular light combination. The UV-pB combination is used in two different scenes: with 5 color stripes, K, R, G, B, Y [denoted by UV-pB (5)], and with 6 color stripes [a gray stripe, Gy, is added to the latter one, to model a larger dynamic range; Gy reflectance can be seen in Fig. 4.2(b), Gy curve]. For combination Na-pG (background produced by sodium light and green fringes by FP projector), object comprises only 4 stripes.

For Fig. 4.8(a), minimum and maximum standard deviations correspond to 0.03 mm [B stripe, UV-pB(5) light combination] and 0.47 mm [R stripe, W-Y(1p) light combination], respectively. On the other hand, for Fig. 4.8(b), they are 0.01 mm (R pigment, Na-pG) and 0.19 mm (K pigment, IR-pB), respectively.

Difficulties arising from dealing with large dynamic ranges can be visualized by comparing the two cases UV-pB(5) and UV-pB(6), where the same light

combination is used. As seen from Figs. 4.8(a) and 4.8(b), performance of UV-pB light combination is superior for an object with 5 colors to an object with 6.

Following the afore-mentioned criterion for proper selection of light source, we can observe from Fig. 4.2(b) that a light source emitting close to 590 nm may be a candidate for the technique, since light of this wavelength is reflected almost equally by black, red, green and blue stripes. This circumstance is analyzed and corresponding results are displayed by the green curves in Figs. 4.8(a) and 4.8(b). As noticed, Na-pG turns to be one of the best light combinations, as long as the scene does not include white and yellow shades, which would enlarge the dynamic range as to cause saturation. For this light combination, Na-pG, DIC and FP signals are detected on red (via crosstalk) and green channels, respectively. Moreover, if in this case, blue fringes are used, i.e. Na-pB, similar results are obtained (fringe pattern should be detected on green channel via crosstalk).

Considering all tested light combinations, performance of FP (error, 3.4%) is higher than that of DIC (error, 10.6%). This result is contrary to what was found for a black-and-white object [11]. The order of the degree of difficulty to measure three-dimensional displacement, considering the pigment colors, is K (error, 6.7%), G (5.7%), R (4.2%), B (3.1%), Y (2.2%). With regard to light combinations, the order of accuracy is Na-pG (error 1.2%), UV-pB(5) [1.5%], UV-pB(6) [2.6%], Y-B(2p) [4.2%], ledR-pB (7.2%), IR-pB (7.6%), W-Y(1p) (24.8%). The most appropriate light combination for analysis of multi-colored objects, overall, is UV-pB. For this latter light combination, a fuller analysis of displacement accuracy is given in Section 4.6.

With reference to the UV-pB light combination, in Fig. 4.8(c) we present some additional information about its contrast realization, for both neutral and multi-colored objects. In that figure, black lines designate FP contrast results and red lines, DIC contrast (the scales of DIC and FP are unrelated). Two cases of multi-colored objects are shown: an object with 5 colors, case (5), indicated by green markers, and an object with 6 colors –a gray stripe is added to the case of 5 colors, case (6), indicated by red markers–. For this type of objects, as described in Sec. 4.4, one registered image is separated into individual images associated with colors present in the scene (which are designated by the abscissa), and then contrast calculation is done. On the other hand, for neutral objects, images of individual colors are taken and no separation is required; the two associated plots with neutral objects are indicated by blue markers. As it can be observed, the largest contrast is

obtained for neutral objects, and the lowest, for case of 6 colors. This result is related to differences in the dynamic range of the three types of scenes.

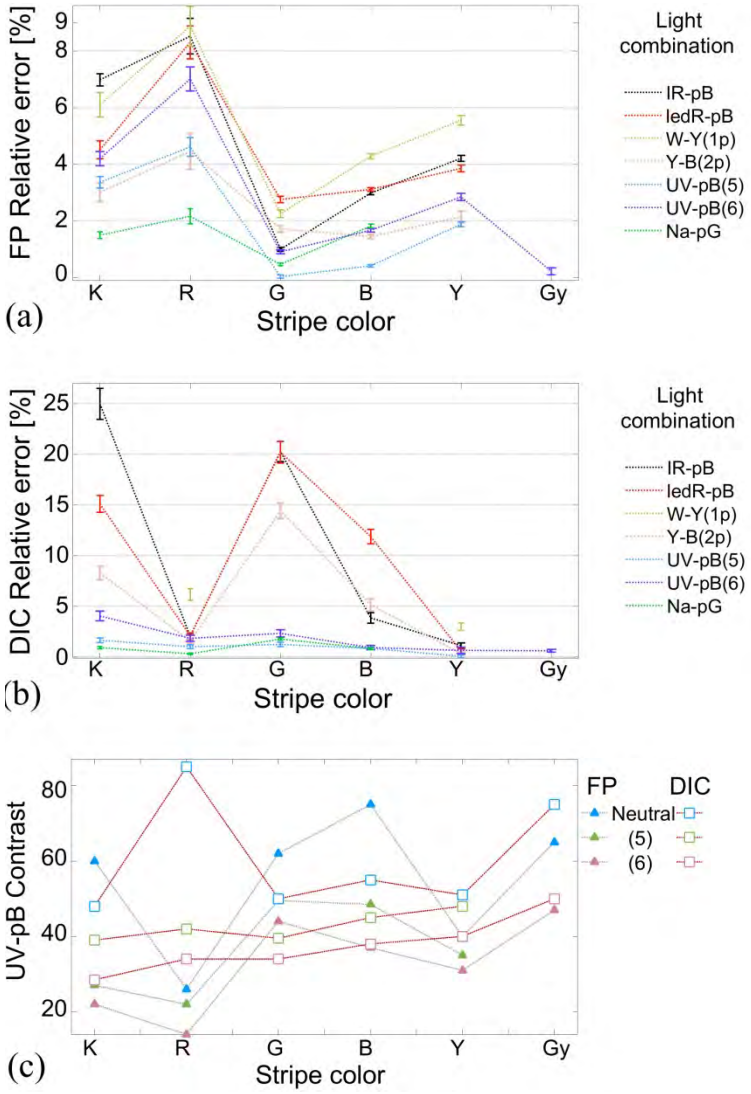

Fig. 4.8. Accuracy of displacement measurement in multi-colored objects. Percentage absolute relative error, (a) out-of-plane (FP) –bars indicate standard deviation– and (b) in-plane (DIC). (c) Contrast evaluation (arbitrary units). The minimum and maximum standard deviations for (a) and (b) are given in the text.

As pointed out in Section 4.4, one-projector configurations show low performance in DIC. For example, even for the best one-projector configuration, [W-Y(1p)], for some stripe colors, the errors are so large that they are not displayed in Fig. 4.8(b).

4.6 Experimental evaluation of displacement

In this section, we evaluate the performance of FP-DIC in multi-colored objects, when the setup includes the best light combination analyzed in Section 4.4, UV-pB (UV for DIC, and blue fringes from FP projector, for FP); the multi-colored objects correspond to those described in Section 4.4. Experimental measurements of a series of prescribed three-dimensional displacements are done. The optical setup is as that shown in Fig. 4.1; separate FP and DIC light sources are incorporated. Values of the distinct parameters of the setup correspond to those described in Sec. 4.4. Three distinct values of displacement are tested: 0.25 mm, 0.5 mm and 1 mm (for both FP and DIC). For each case, the total numbers of displacement steps are 40, 20 and 10, respectively.

Figure 4.9 includes the resulting absolute percentage relative errors, indicated by the ordinate of the plot, along with the standard deviation; standard deviation is indicated by green small bars positioned over main bars. The abscissa designates the stripe colors that form the multi-colored object; two sets of stripe colors are included: one for a 5-stripe object (K, R, G, B, and Y), and another for a 6-stripe object (K, R, G, B, Y, and Gy); the rightmost color, W, is associated with measurements in a neutral white object, which serves as a reference. For the latter case, W, FP and DIC light sources correspond to FP and DIC projectors (which are spatially separated); they respectively generate, in a non-simultaneous way, a pattern of black-and-white fringes and a uniform white light field.

Some interesting features can be observed from the results. First, accuracy of DIC reference measurement (white object, W, illuminated by separated projectors) is larger than that found previously in [11]; this arises from the fact that DIC source is detached from FP source. Besides, DIC performance of this case is higher than that of FP, as found in [11] –compare the rightmost groups of bars of Figs. 4.9(a) and 4.9(b)–. Second, for DIC, the greater the displacement, the less the relative error. Third, overall accuracy for multi-colored objects is on the order of that obtained when only one projector illuminates a neutral object, about 1.5% [3]. Fourth, performances of DIC and FP are similar. And finally, by comparing the behavior of results in Fig. 4.9 and Fig. 4.8(c), accuracy and contrast show a direct relationship.

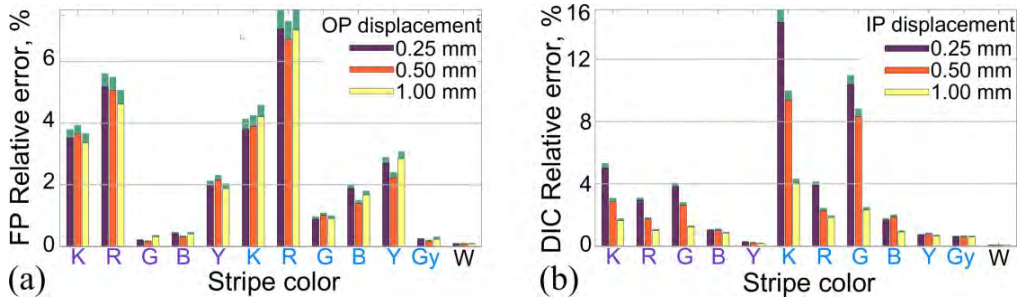

Fig. 4.9. Absolute percentage relative error of three-dimensional displacement in multi-colored objects. (a) Out-of-plane (OP) displacement from FP; minimum and maximum values of standard deviations are 0.012 mm (for W, displacement step of 1.0 mm) and 0.28 mm (R, 6 colors, displacement step of 1.0 mm); and (b) in-plane (IP) displacement from DIC –standard deviation is within 0.008 mm (for W, displacement step of 1.0 mm) and 0.1 mm (K, 6 colors, displacement step of 0.25 mm).

It is worth pointing out that on obtaining the results related to multi-colored objects, the camera gamma value is adjusted as described at the end of Sec. 4.4; as noted, this implies that the intensity of low-reflectance pixels is reinforced. Additionally, gains of channels are chosen as indicated in Sec. 4.4.2.

4.7 Conclusions

We have evaluated the performance of the FP/DIC technique, when applied to colored objects, by measurements of contrast and displacement accuracy. When analyzing a set of different neutral-colored objects, we found out that the best performance is obtained when illuminating the object by a light combination that comprises a red light background, produced by a matrix of LEDs (DIC light source), and a pattern of blue fringes, generated by a projector (FP light source). In this case, for selection of the light sources, their crosstalk, with respect to the camera sensor, should be as weak as possible. Similarly, when dealing with multi-colored objects that present high dynamic ranges, the recommended combination of light sources is UV for DIC and pure blue fringes, for FP. Regarding this case, the key point for selecting the light sources, is that all colors comprising the object should reflect as similar as possible the light spectra.

In general, to optimize the FP-DIC setup, light sources for each technique should be spatially separated. One advantage of this type of configuration is the possibility to select independently both optimum angles of illumination and illumination power for each technique, what may increase flexibility and accuracy of the setup. The optimal

setup allowed us to measure three-dimensional displacement in dynamic events, by using only one image.

4.8 References

1. M. A. Sutton, J. H. Yan, V. Tiwari, H. W. Schreier, and J. J. Orteu, "The effect of out-of-plane motion on 2D and 3D digital image correlation measurements," Opt. Lasers Eng., **46**, 746–757 (2008).
2. L. F. Sesé, P. Siegmann, F. A. Diaz, and E. A. Patterson, "Simultaneous in-and-out-of-plane displacement measurement using fringe projection and digital image correlation," Opt. Lasers Eng. **52**, 66–74 (2014).
3. D. Caspi, N. Kiryati, and J. Shamir, "Range imaging with adaptive color structured light," IEEE Trans. on Pattern Analysis and Machine Intelligence, **20**(5), 470–480 (1998).
4. P. S. Huang, Q. Hu, F. Jin, and F. P. Chiang, "Color-encoded digital fringe projection technique for high-speed three-dimensional surface contouring," Opt. Eng. **38**(6), 1065–1071 (1999).
5. M. Padilla, M. Servin, and G. Garnica, "Fourier analysis of RGB fringe-projection profilometry and robust phase-demodulation methods against crosstalk distortion," Opt. Express **24**(14), 15417–15428 (2016).
6. Z. Zhang, C. E. Towers, and D. P. Towers, "Time efficient color fringe projection system for 3D shape and color using optimum 3-frequency selection," Opt. Express **14**(14) 6444–6455 (2006).
7. CMOSIS image sensors, "CMV2000 Datasheet v3.2," 2012.
8. E. Peli, "Contrast in complex images," J. Opt. Soc. Am. A **7**(10), 2032–2040 (1990).
9. K. J. Gasvik, *Optical Metrology*, (John Wiley and Sons, 2003).
10. P. Siegmann, V. Alvarez-Fernandez, F. Diaz Garrido, and A. E. Patterson, "A simultaneous in- and out-of-plane displacement measurement method," Opt. Lett. **36**(1), 10–12 (2011).
11. C. Mares, B. Barrientos, and A. Blanco, "Measurement of transient deformation by color encoding," Opt. Express **19**, 25712–25722 (2011).
12. L. F. Sesé, P. Siegmann, F. A. Diaz, and E. A. Patterson, "Simultaneous in-and-out-of-plane displacement measurement using fringe projection and digital image correlation," Opt. Lasers Eng. **52**, 66–74 (2014).
13. B. Barrientos, M. Cerca, J. Garcia-Marquez, and C. Hernandez-Bernal, "Three-dimensional displacement fields measured in a deforming granular-media surface by combined fringe projection and speckle photography," J. Opt. A: Pure App. Opt., **10**, 104027 (2008).

5 Application examples

We present two application cases related with the optimized FP-DIC setup, following the findings of Chapter 4. The two examples fall in the field of geology.

5.1 Compression model

The experiment is regarded to the analysis of geological models, when subjected to external compressive forces [1]. These types of experiments serve to model the morphological spatio-temporal evolution of the Earth's crust while subjected to particular natural conditions. As shown in Fig. 5.1, the model is formed by 5 vertical layers of colored granular media (average diameter of 0.5 mm), Fig. 5.1(a). The shape of the initial state of the object corresponds to a box of volume 30 cm x 15 cm x 3 cm (length, width, height). In these type of experiments, it is customary the use of colored layers for easy visualization of the deformation. Compression is applied as in [1], i.e., by an advancing wall made of plastic, which is driven by a stepper motor (at a speed of 1 mm/s). The object is illuminated by UV-pB combination (parameters of the setup take values as described in Sec. 4.4.2). The image of the object, at its reference state, when illuminated by UV-pB is shown in Fig. 5.1 (b). From this latter image, we obtain the separated images (FP image from green channel and DIC image from red channel), which are shown in Figs. 5.1(c) and 5.1(d). Figures 5.1(e) and 5.1(f) show the components of displacement at two different states: length shortenings of 9.7% and 21.6%, respectively; in these images, the out-of-plane and in-plane displacements are represented by color map and vectors, respectively [for Fig. 5.1(e), the maximum vector represents 0.26 mm, and for Fig. 5.1(f), 0.28 mm; the similarity of these values reflects the constancy of displacement of the moving wall]. Horizontal cross-sections of the two latter images are shown in Figs. 5.1(g) and 5.1(h), for the central row; the first cross-section plot depicts the out-of-plane component and the second, the horizontal in-plane component; evolution of the deformation is clearly noticed. For the out-of-plane displacement, the reference state is fixed and corresponds to the undeformed state; and for the in-plane displacement, the reference is continuously updated; i.e., the reference image corresponds to the image preceding the image under analysis (camera recording speed is 1 fps). As observed, the largest displacements occur near the compressing wall. Further, small rotations of the surface appear due to the interaction of the sand and the side walls

of the container (this in turn produces a faster movement of the central part of the foreland). As noticed, the maximum in-plane displacement is on the order of one third of the wall displacement. This difference arises from the fact that the movement of the wall generates both in-plane and out-of-plane components of displacement of the sand. The out-of-plane movement is reflected as accumulation of sand near the wall. The movement of the sand resembles that of a solid object (a plateau), that only gains height with compression but does not flow horizontally easily —this effect can also be observed from the in-plane maps, where movement of the sand close to the far edge is relatively small.

In summary, by using an appropriate light combination, multi-colored objects may be analyzed by using only one registered image, simplifying the standard procedure of using multi-exposure methods, as in [2-4].

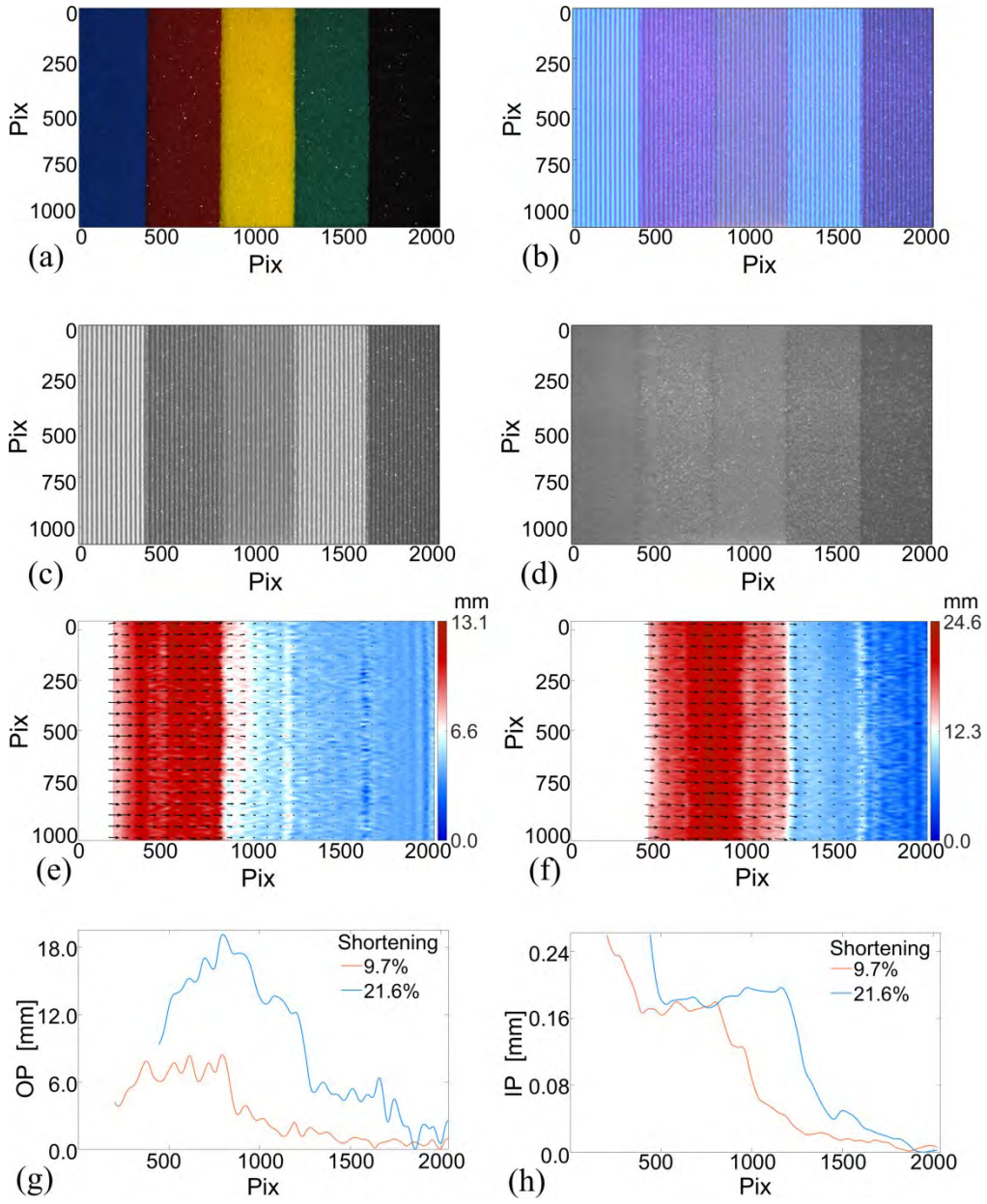

Fig. 5.1. Three-dimensional displacement in a geological model. (a) Real specimen. (b) Specimen illuminated by UV-pB. From Fig 5.1(b), (c) FP image and (d) DIC image. (e) Three-dimensional displacement at length shortening of 9.7%. (f) Three-dimensional displacement at length shortening of 21.6%. Cross-sections of Figs. 5.1(e) and 5.1(f): (g) Out-of-plane component and (h) horizontal in-plane component.

5.2 Landslide

Granular avalanches are common phenomena in nature, and when they occur on a large scale, represent major geological hazards [5-6]. Examples of granular avalanches are pyroclastic flows or debris flows [7-8]. Experimental knowledge of the detailed kinematics of these phenomena is of great importance, because it allows us developing more detailed rheological models, as well as more efficient simulation algorithms. Indirectly, the observations made in experiments can also contribute to an efficient hazard manage for civil protection.

The experimental granular materials simulating avalanches are made of natural mixtures of volcanic materials with polidisperse grain sizes, and the physical experiments are performed in a flume of 1 m long [9]. The flume consists of a Plexiglas ramp with inclination angle of 38° and with lateral confining walls. A mixture of low density granular material (pumice, particle mean diameter of 2 mm) of 1.5 kg is thrown at the upper part of the ramp. The mean velocity on the ramp plane is about 2.5 m/s.

A yellow fringe pattern with a 6.45 mm period, embedded in a white background, is projected on the ramp. Digital images are recorded using a Photron MiniUX100 camera at 1000 fps. In this case, only one projector is used, basically because the texture is relatively high and it has a neutral color (gray). The FP image is contained on the blue channel and the DIC image on the red channel. Both the camera and the projector are placed at the same distance from the ramp (1050 mm) and the projection angle is 14.7°. The optical axis of the camera is perpendicular to the ramp plane and the total area of analysis is 710×105 mm^2 (close to the bottom edge). The cross-sectional area of the canal is 105x105 mm^2.

In Fig. 5.2 we present the raw images related to one measurement example of displacement of a landslide. Sets of 4 images correspond to one instant as the slide starts moving from the upper part and reaches the bottom edge. Units are mm. The color image of each set of images corresponds to the recorded image. When this image is separated, produces the FP and DIC images (blue and red images, respectively). Besides, an encoded RGB color image is included; it is formed as follows, the blue/green channel is associated with the reference speckle image and the red channel with the displaced speckle image. This latter image serves to readily visualize the instantaneous motion (1 ms between consecutive images) of the sand.

The recording time, in ms, from the onset of the slide, is indicated by the yellow number.

As shown by the FP images, zones corresponding to the slide front become too noisy because of the high kinetic energy of the particles and the strong interaction between neighbor particles (random jumping of around 3 cm is seen). The resulting information from the noisy zones is then not reliable.

At the onset of the avalanche (within the field of view of the camera, whose edge is at 30 cm below the top edge of the flume), the free surface of the thrown material (pure pumice) rapidly increases. At about 380 ms, the flume cavity gets full, and from then onwards, a stable level of sand is maintained, until draining takes place, at about 420 ms. At later times, not shown, the material is accumulated at the bottom edge and the level of the free surface of the slide starts increasing again.

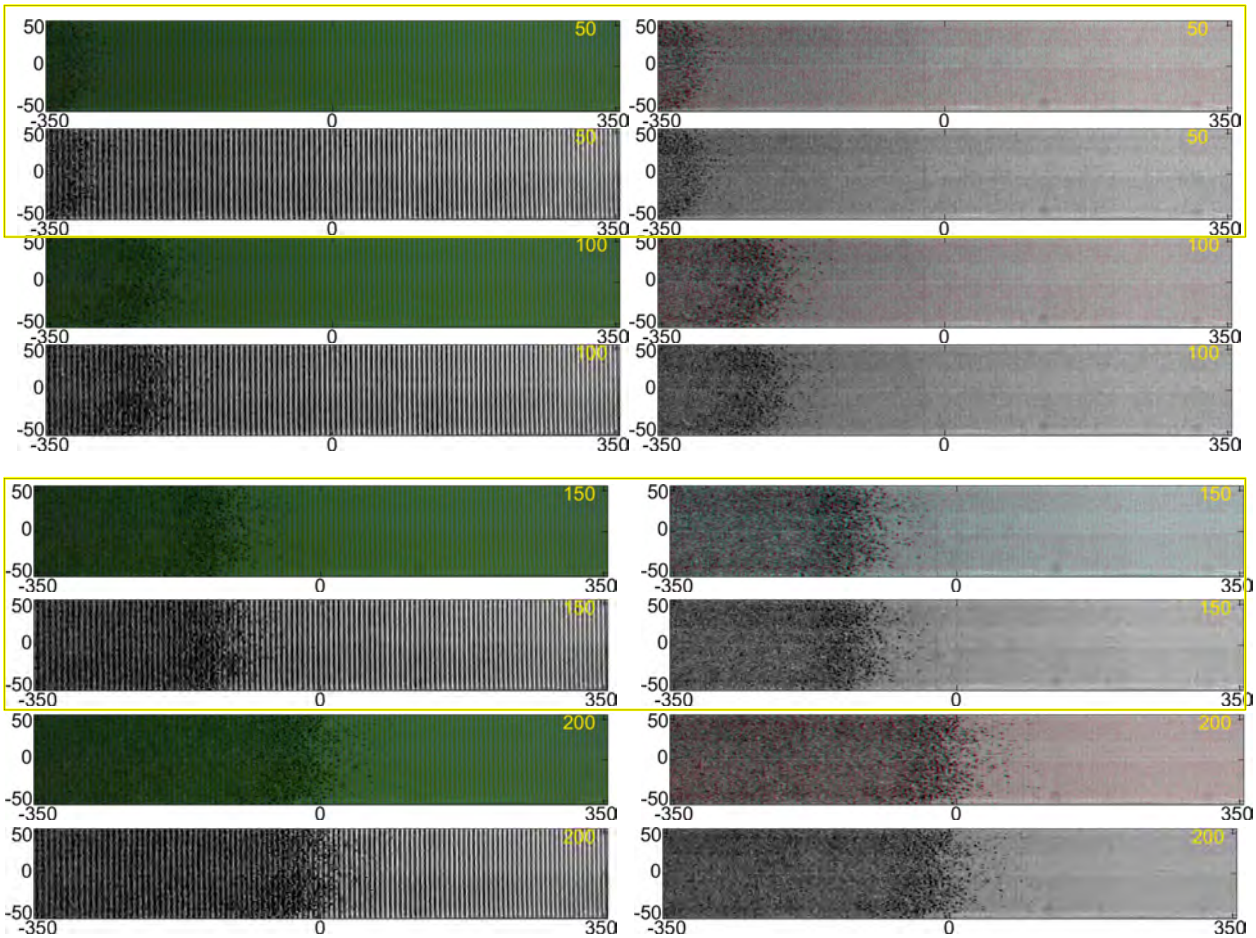

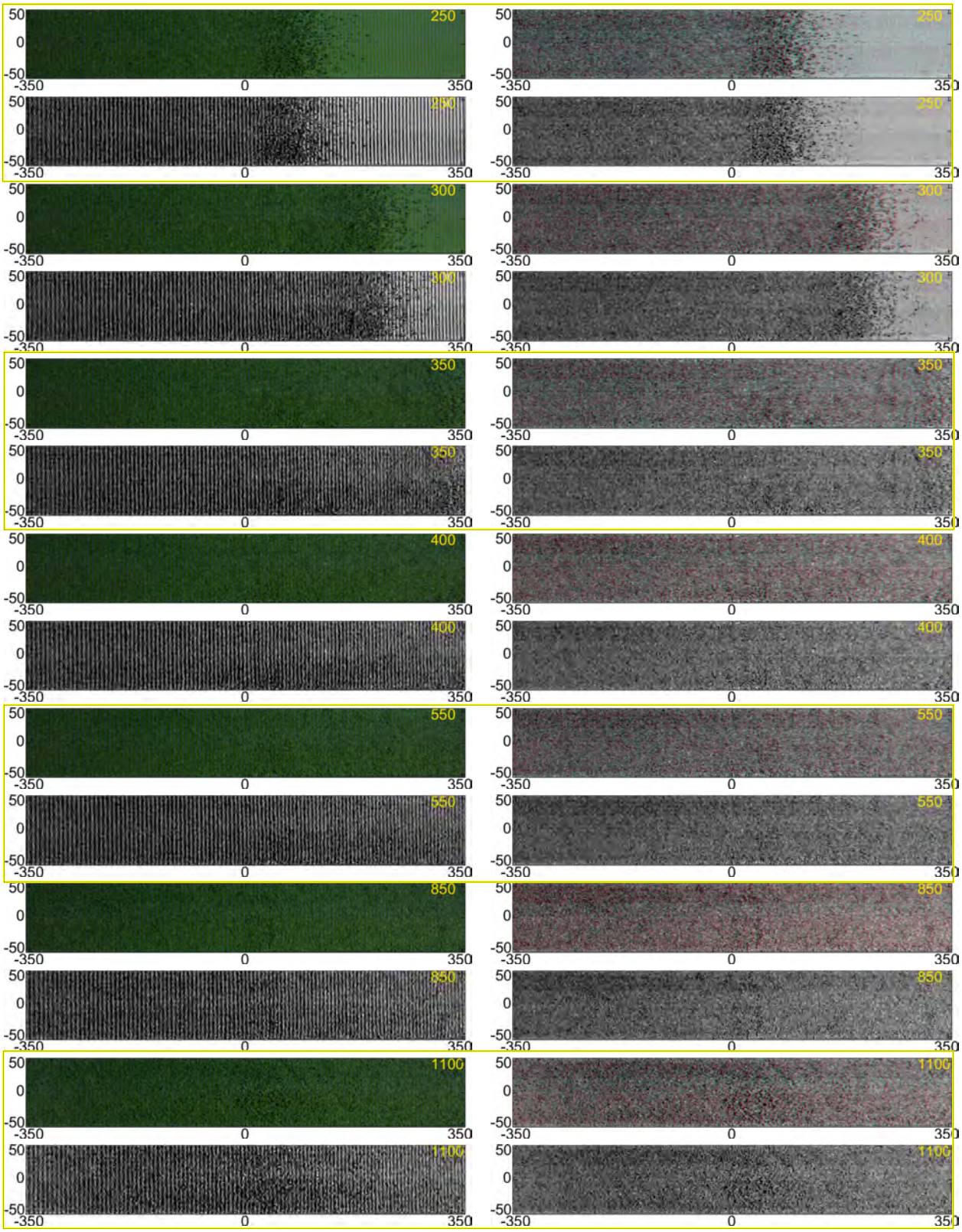
250
250
250
250
300
300
300
300
350
350
350
350
400
400
400
400
550
550
550
550
850
850
850
850
1100
1100
1100
1100
50
0
-50
-350
0
350

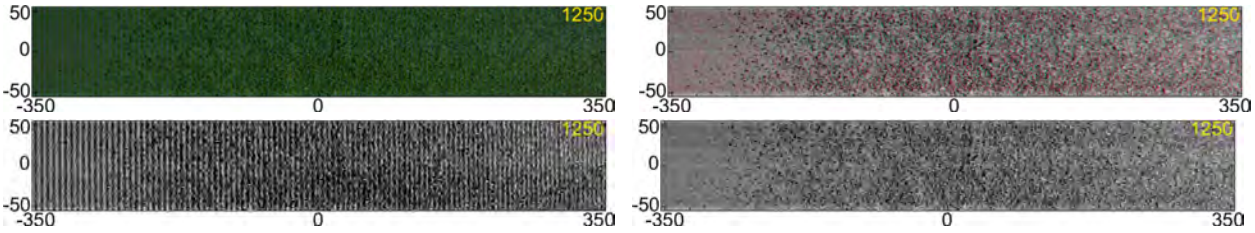

Fig. 5.2. Transient phenomena, a slide on a flume. Description of figures is in the text.

The FP and DIC images in Fig. 5.2 are used to obtain the displacement maps that are shown in Fig. 5.3. In the plots, the minimum and maximum values of the in-plane, ip, speed (displacement) is included, and the maximum value of the out-of-plane displacement (op) as well. For the overall experiment, the maximum out-of-plane displacement is about 30 mm (150 ms), and the maximum in-plane speed, 3.1 m/s (at 350 ms, which sharply precedes the time at which the cavity gets full).

Considering that the location of the recipient of the sand is 25 cm above the flume and applying a free-fall model, the mixture impinges on the ramp 226 ms after being released, and with a speed of 2.214 m/s. Then, 30 cm below, along the ramp direction, the velocity is (at the left edge of the field of view) 2.341 m/s; this value is the initial velocity of the mixture at the left edge of the field of view, see Fig. 5.3(a); the measured value is about 2.2 m/s, which is slightly less than the theoretical one. Then, it takes 230 ms to get to the right edge (bottom edge) —the measured value is around 350 ms, see Fig. 5.3(g)—; the expected speed is 3.733 m/s, and the measured value is around 3.1 m/s. The discrepancies in values arise mainly from friction losses.

Note that the difference in maximum and minimum velocity increases as the flow evolves. Also, the gradient of speed due to the effect of gravity is readily noticed. This speed gradient smooths out any lump/pit of the free surface, which tends to produce flat surfaces.

In Fig. 5.4 we include corresponding cross-sections of Fig. 5.3, along a horizontal line —located in the middle of the images.


50 ms
z [mm]
0
-300
-200
-100
y [mm]
0
100
200
300
50
0
-50
x [mm]
op [mm]
30.0
20.0
10.0
0.0
ip, MIN MAX, [0.0, 2.2] m/s
op, MAX, 12.5 mm

(a)


100 ms
z [mm]
-300
-200
-100
y [mm]
0
100
200
300
50
0
-50
x [mm]
op [mm]
30.0
20.0
10.0
0.0
ip, MIN MAX, [0.0, 2.3] m/s
op, MAX, 27.1 mm

(b)

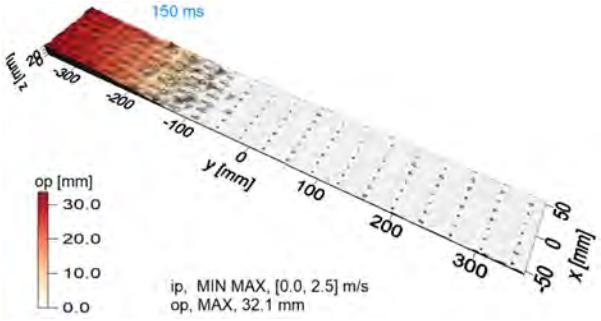
150 ms
z [mm]
-300
-200
-100
y [mm]
0
100
200
300
50
0
-50
x [mm]
op [mm]
30.0
20.0
10.0
0.0
ip, MIN MAX, [0.0, 2.5] m/s
op, MAX, 32.1 mm

(c)

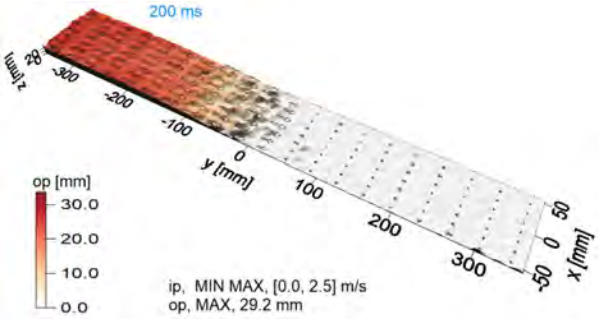
200 ms
z [mm]
-300
-200
-100
y [mm]
0
100
200
300
50
0
-50
x [mm]
op [mm]
30.0
20.0
10.0
0.0
ip, MIN MAX, [0.0, 2.5] m/s
op, MAX, 29.2 mm

(d)

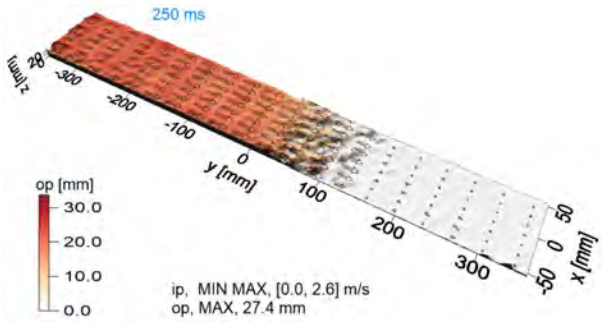
250 ms
z [mm]
-300
-200
-100
y [mm]
0
100
200
300
50
0
-50
x [mm]
op [mm]
30.0
20.0
10.0
0.0
ip, MIN MAX, [0.0, 2.6] m/s
op, MAX, 27.4 mm

(e)

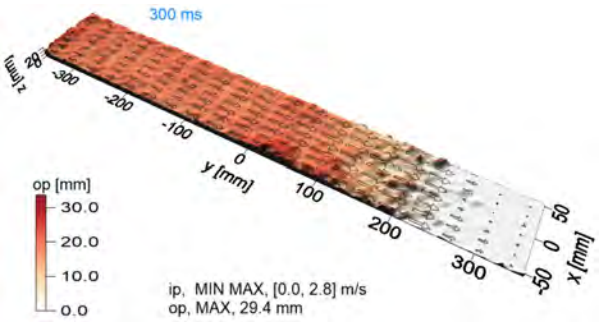
300 ms
z [mm]
-300
-200
-100
y [mm]
0
100
200
300
50
0
-50
x [mm]
op [mm]
30.0
20.0
10.0
0.0
ip, MIN MAX, [0.0, 2.8] m/s
op, MAX, 29.4 mm

(f)

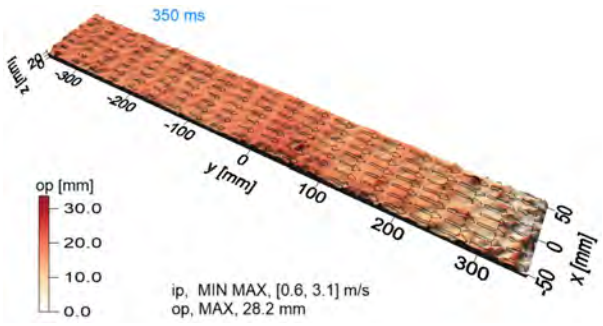

(g)

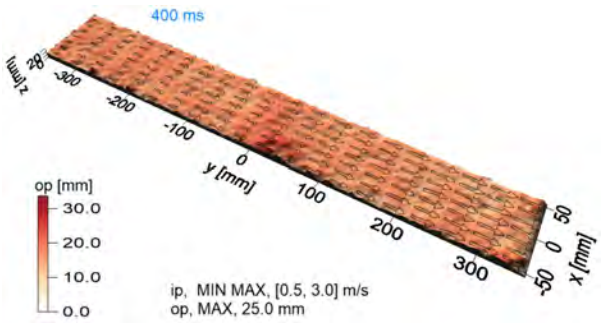

(h)

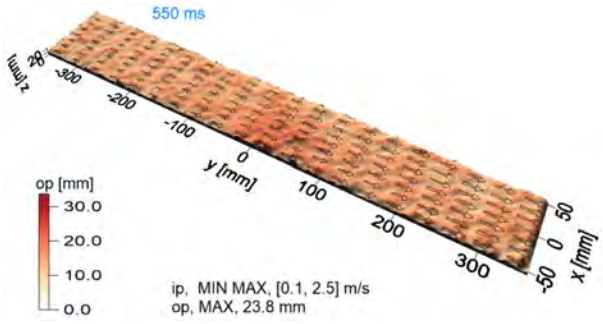

(i)

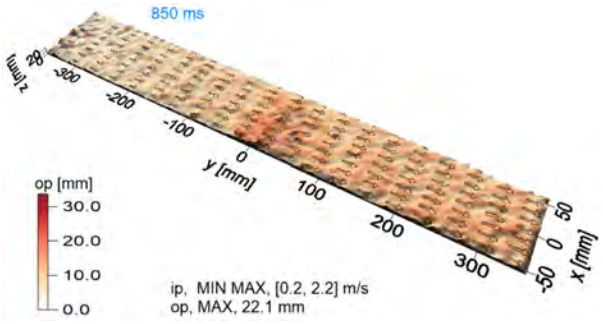

(j)

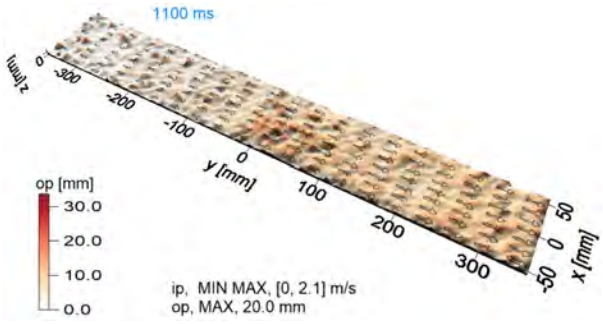

(k)

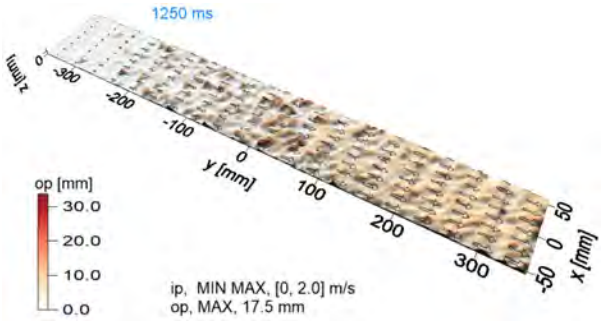

(l)

Fig. 5.3. Three-dimensional displacement at several time positions (indicated by blue numbers).

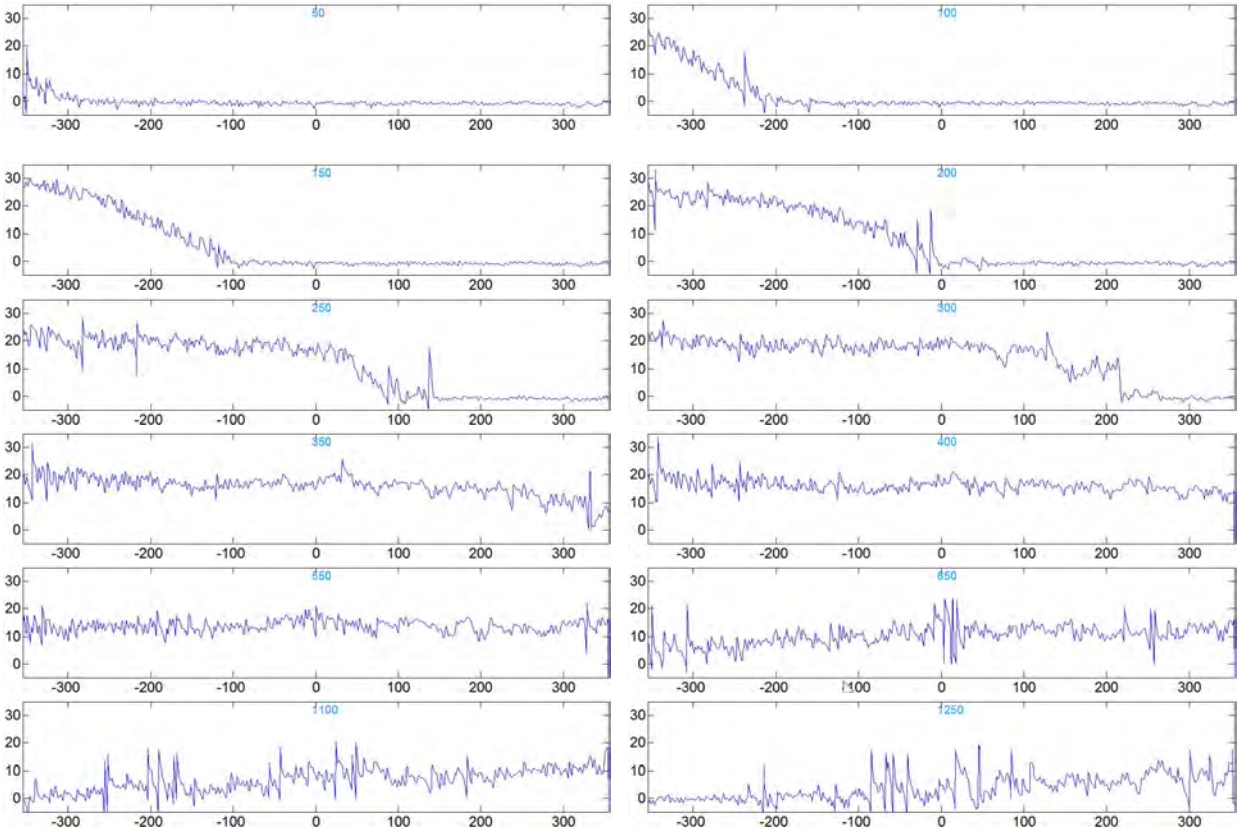

Fig. 5.4. Cross-sections of corresponding figures in Fig. 5.3.

At the beginning of the flow, the displacement of particles in the front is characterized by rolling and random leaping and their chaotic behaviors induce a high variation in the measurements.

The complete temporal displacement behavior of the avalanche is presented in Figs. 5.5(a) and 5.5(b). Three plots are reported in Fig. 5.5(a), indicated by Vol, Dev and MAX; the x-axis represents time in ms. Variable Vol indicates the average of the height distribution; therefore, it is proportional to the current granular material volume in the flume (the time at which the cavity gets full is clearly indicated by the position of the maximum peak, at about 380 ms). Additionally, Dev designates the standard deviation of the current height distribution; this parameter enables us to have an insight into the spatial irregularities of the height distribution. As expected, this curve shows a parabolic-like part that coincides with the filling of the cavity as well (when the cavity gets full and when it is drained, the leaping decreases considerably).

Curves MAX refer to the maximum of height; this parameter is calculated by taking the mean of the largest 5000 values of height —the reason to take the average is to smooth the strong variations of the maximum of height due to the random leaping of the deformation front. We notice that the maximum of height is reached at about 150 ms. The missing data at the start of the height curve reflects the existence of instabilities of the granular material (random leaping).

On the other hand, in Fig. 5.5(b) two more plots are illustrated. The first one, mdz, indicates the average of the differences between consecutive measurements separated by 2 ms —it corresponds to the spatial mean of a temporal derivative. This latter parameter helps us visualize temporal changes of the height distribution. The other plot, sddz, refers to the standard deviation of the temporal derivative; it serves to visualize time instabilities of the height distribution, which in Fig. 5.5(b) take maximum values when filling up and emptying of the cavity.

Another type of material is tested: andesite (this is denser than pumice, 2.5 and 0.64 kg/m^3, respectively). The results regarding this granular material (average diameter of 2 mm) are presented in Figs. 5.5(c) and 5.5(d). By comparing the measurements, slight differences come to light: (a) the cavity filling time, which is directly related to the amplitude of the velocity (they practically coincide), (b) the level of instabilities, which depends on the coefficient of restitution, COR — ratio of final to initial relative speed between two colliding objects; ranges from 0 to 1, where 1 is for a perfectly elastic collision— of the material (andesite shows the greatest level, COR of 0.87 compared with 0.24 [10, 11]), (c) the width of the peak of maximum height, which is also linked to the COR.

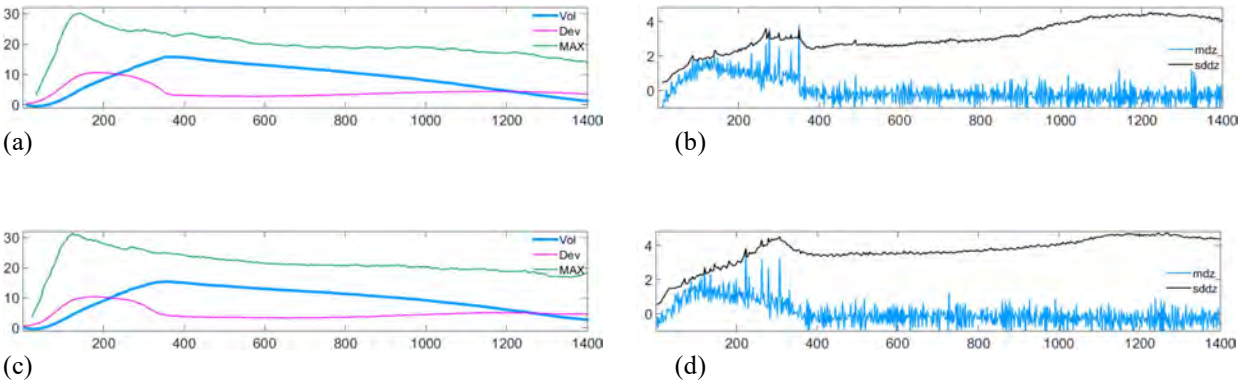

Fig. 5.5. Temporal dynamics of avalanches. Pumice, (a) spatial behavior, (b) temporal variations. Andesite, (c) spatial behavior, (d) temporal variations.

Finally, we show the results of displacement regarding another granular material: a mixture of cornstarch (mean particle diameter, 30 μm [12]) and white stone (mean diameter of 4 mm), with a proportion 35-65 in volume. The resulting dynamics is shown in Fig. 5.6. Firstly, the maximum speed is on the order of 1.5 m/s, less than before. The cornstarch tends to agglomerate and to slow down the flow, which yields some lumps that are observed during the whole event. Besides, we can notice the presence of a smaller gradient of velocity than in the previous experiments, but enough to also flatten any irregularities of the surface, such as the lumps. Besides, notice that in the neighborhood of the main lump the velocity vectors show a larger vertical component than the previous experiment. Also, the gradient of velocity, along the flume, is noticed to be smaller before the lumps, than after them.

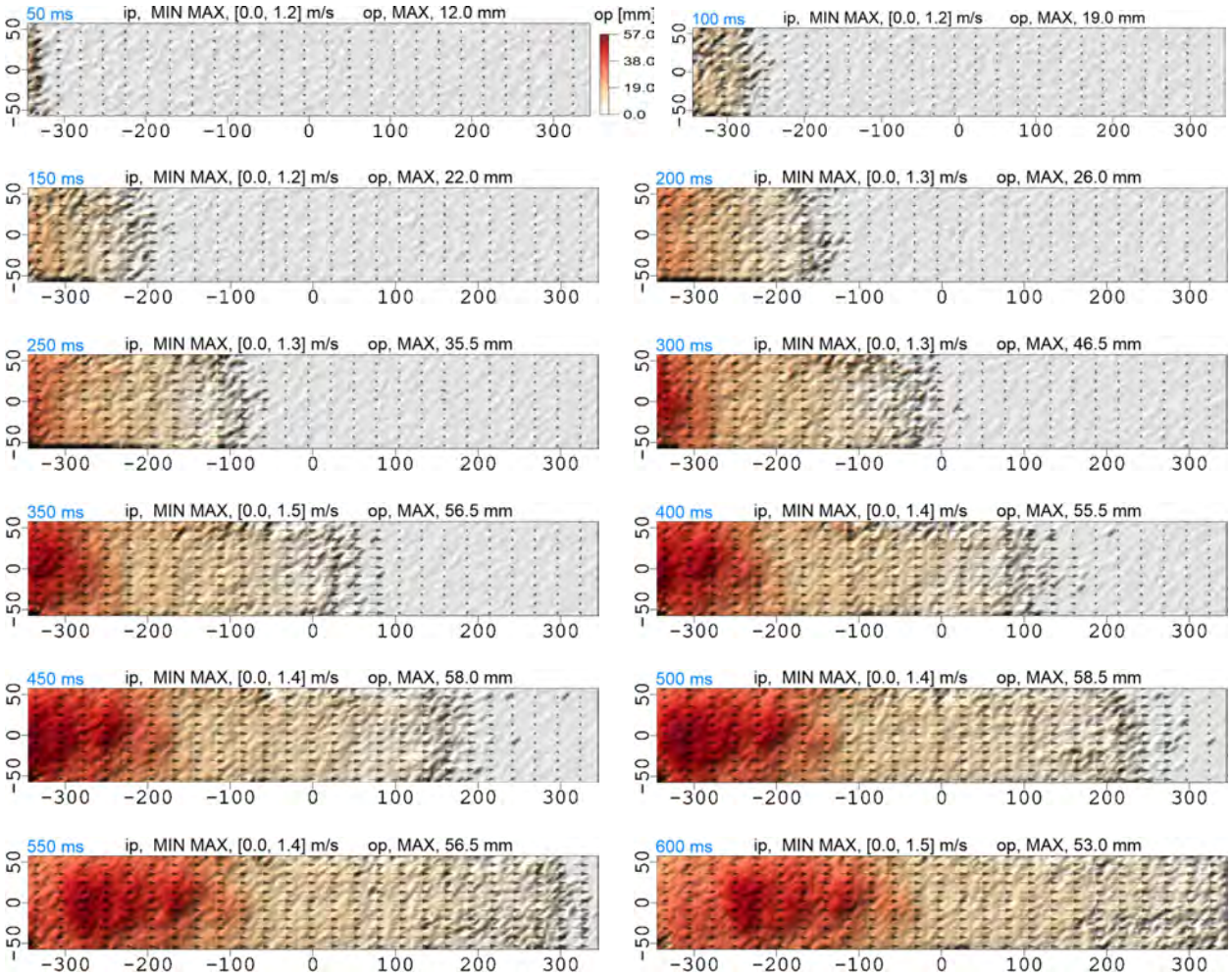

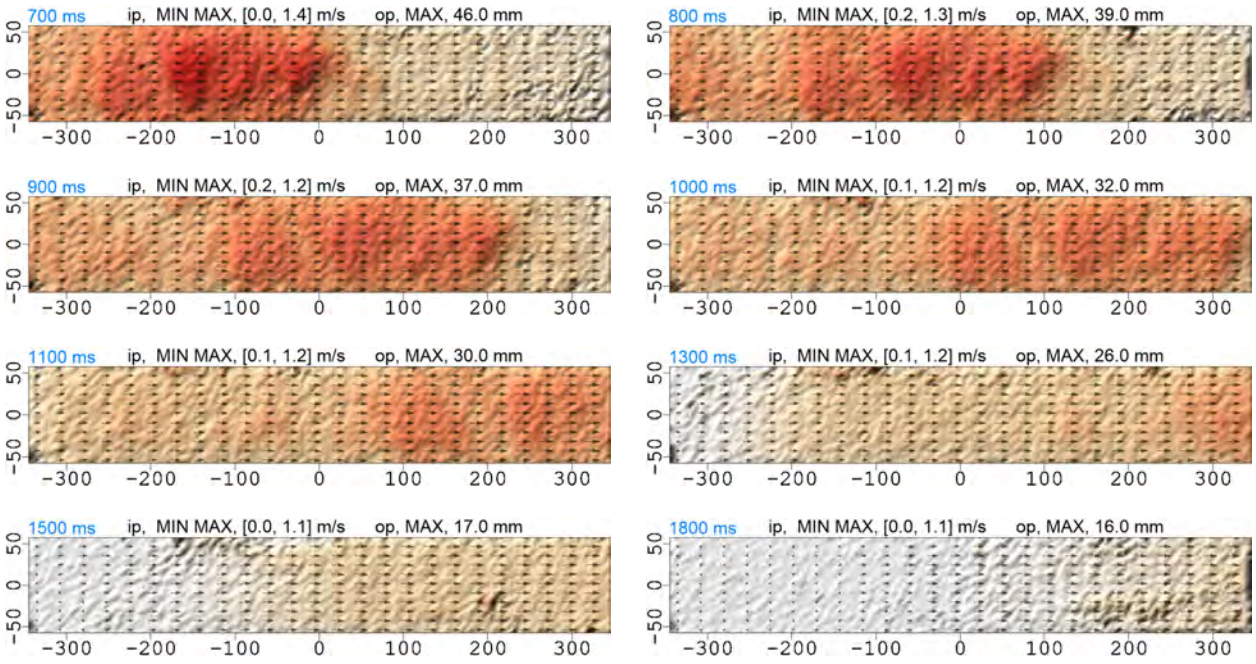

Fig. 5.6. Temporal dynamics of an avalanche with a mixture of cornstarch and white rock.

5.3 Conclusions

We showed the feasibility of the proposed technique, FP-DIC, for the measurement of transient phenomena, such as compression of geological models and modeling of landslides. As shown, by these types of experiments, we may characterize materials that are used in geology and also obtain the temporal behavior of the phenomena.

This study may provide detailed information on grain size segregation and velocity changes inside the avalanche during its development by laterally observing the avalanche. Two flat mirrors at 45° are incorporated into the setup (placed at the sides of the flume) to accomplish this latter point.

5.4 References

1. B. Barrientos, M. Cerca, J. Garcia-Marquez, and C. Hernandez-Bernal, "Three-dimensional displacement fields measured in a deforming granular-media surface by combined fringe projection and speckle photography," J. Opt. A: Pure App. Opt., **10**, 104027 (2008).
2. A. R. Varkonyi-Koczy, A. R. Rovid, and T. Hashimoto, "Gradient based synthesized multiple exposure time color HDR image," IEEE Trans. on Instrumentation and Measurement, **57**(8), 1779–1785 (2008).
3. D. Skocaj, A. Leonardis, "Range image acquisition of objects with non-uniform albedo using structured light range sensor," in *Proceedings of IEEE 15th International Conference on Pattern Recognition (ICPR 2000)*, (IEEE, 2000), pp. 778–781.

4. B. Chen and S. Zhang, "High-quality 3D shape measurement using saturated fringe patterns," Opt. Lasers Eng., **87**, 83–89 (2016).
5. R. Dikau, D. Brunsden, L. Schrott, and M. L. Ibsen, M.L., *Landslides recognition: identification, movement and causes*. Ed. John Wiley & Sons, New York (1996).
6. M. Jakob and O. Hungr. *Debris-flow Hazards and Related Phenomena*. Ed. Springer, Berlin (2005).
7. D. Sarocchi, R. Sulpizio, J. L. Macías, and R. Saucedo, "The 17 July 1999 block-andash flow at Colima volcano: new insights on volcanic granular flows from textural analysis," Journal of Volcanology and Geothermal Research, **204**, 40-56 (2011).
8. R. Sulpizio, L. Capra, D. Sarocchi, R. Saucedo, J. C. Gavilanes, and N. Varley, "Predicting the block and ash flow inundation areas at Fuego de Colima volcano (Colima, Mexico) based on the present day status," Journal of Volcanology and Geothermal Research, **193**, 49-66 (2011).
9. C. Mares, B. Barrientos, M. Cerca, D. Sarocchi, and L. A. Rodriguez, "Fringes projection for 3D analysis of experimental dry granular avalanches", Elger, K; Haug, Ø. T.; Ritter, M. C. (Eds), Proceedings of GeoMod2014 – Modelling in Geosciences: Programme and Extended, Potsdam, 459-463 (2014).
10. https://www.rocscience.com/help/rocfall/webhelp/baggage/Dynamic_Friction_Rolling_Friction_Table.htm, consulted on September 13, 2017.
11. B. Cagnoli, M. Manga, and M. Boone, "Kinetic Energies in Oblique Pumice-Pumice Impacts and Coefficient of Restitution," AGU Fall Meeting Abstracts, (2002).
12. G. A. Hareland, "Evaluation of flour particle size distribution by laser diffraction, sieve analysis and near-infrared reflectance spectroscopy," Journal of Cereal Science, **20**, 183-190 (1994).

6 Conclusions and future work

6.1 Conclusions

We have presented a theoretical and experimental analysis of a technique that combines fringe projection and digital image correlation. This technique can yield the three components of displacement by using only one image. The information needed by the techniques is encoded on the RGB channels of a color camera: first, the color encoding is done by using spectrally separated light sources, which may be part of only one projected image or of two projected separated images; then, the registered image is separated into its three channels by software; two of these images are then used for analysis. Then, FP-DIC can yield the in-plane and out-of-plane displacement components, in a simultaneous way, what enables us to study transient phenomena, such as avalanche models.

A useful future of the method is that the object does not have to be prepared in advance, such as application of sprayings or surface painting. However, when the texture of the object is not enough to produce a well-developed white speckle pattern, DIC does not produce confident results. To alleviate this problem, we incorporated a second source of light, so that the texture is boosted. In this case, unlike the quasi-normal illumination of FP, almost grazing illumination may be employed to favor the production of spatial structures. Additionally, a second independent illumination source allows us to control the intensity and spectral characteristics of the DIC source, resulting in a technique with the potential to analyze multi-colored objects, and even objects with relatively large dynamic range. The technique can be applied in industrial environments and for engineering objects that are not necessary to be prepared in advance.

The range of displacement is from tenths of micrometers to a few centimeters. On the other hand, the range of object size is from a few mm to a size limited by the power of the light sources. And considering the speed of the camera, the velocity may be from zero to several meters per second.

We applied the proposed technique to the analysis of two typical examples in structural geology: a compression model and a landslide model. As presented, in both cases the complete three-dimensional deformation was successfully measured.

6.2 Discussions

There are several techniques that are able to measure three-dimensional displacement, such as stereoscopy, electronic speckle pattern interferometry and digital holography. However, setups are generally complex, requiring the use of at least 2 cameras or coherent sources of light; or they can only work in ambients free of noise. In the last 5 years, setups have been proposed to use only one camera and with industrial environments. For this purpose, the latest proposals have opted to use color encoding. In this work, we have presented a variation of this latter tendency, where the objects do not need any preparation, such as surface painting. This feature is the main contribution of this work.

The ability to study objects that do not require any previous conditioning potentially widens the application fields, for example the analysis of fine arts objects or the analysis of real mechanical parts, which may contain a large number of colors.

We have shown that the range of measurement of the technique is limited by the size of the projected period, regarding the minimum value of out-of-plane displacement, and the depth of field of the imaging lens, considering the maximum value. The minimum value of the period is mainly connected with the resolution of the graphics card and the digital projector. In our case, the minimum value is about 2 mm for a high-definition projector. If we consider that the resolution for the Fourier method is around 1/20th of the period, then the actual resolution is about 100 μm. On the other hand, for the maximum value, it corresponds to the depth of field, which is approximately 8 cm. The depth of field can be increased by stopping down the aperture of the imaging lens at the expense of the level of light intensity.

With regard to the range of measurement of the in-plane component, the limitations correspond to the resolution of the correlation algorithm (0.1 pix) and one-quarter of the subimage size (generally 24 pix). Hence, the resolution is about 30 μm (for a field of view of 30 cm and 1000-pix image) and the maximum displacement between consecutive images is around 1.2 mm. By considering these last values, the equivalent range of speeds can be estimated. The maximum value of speed can be directly handled via selection of the time between images, hence being capable of dealing with speeds from 0 m/s to 1.2 m/s (for a time between images of 1 ms or equivalently a camera speed of 1000 fps). If larger speeds are to be measured, the time can be lowered, but the light intensity should be proportionally increased.

The light intensity limits the maximum field of view as well. In this respect, FP is more sensitive to this restriction since the throughput of a digital projector is fixed. Unlike this, for DIC, the light intensity may be increased more easily by adding several sources of light.

Finally, considering the range of colors of the object, in principle the scene may contain all colors. This feature is limited, however, by the dynamic range, which is in turn affected by the contrast of lightness of the colors (black-and-white being the limiting case) and the presence of reflections.

6.3 Future work

There are some points that can be met in a further work. With regard to avalanches, there is pending the use of different granular media, and the subsequent identification of dynamic behaviors; one of those to-be-searched features is the apparent formation of periodic fronts, like those observed when water flows along an inclined street. Besides, complete colored-layered models can be now studied, which widens the possibilities for modeling. In the immediate future, the technique will be applied to the measurement of displacement in circular plates subjected to vibration.

Another work that may be carried out is the implementation of other phase techniques, such as phase stepping and wavelet methods.

6.4 Products in the period

Following, we list the principal products achieved during the doctorate period.

6.4.1 Scientific publications (4)

1. C. Mares, B. Barrientos, and R. Valdivia,"Three-dimensional displacement in multi-colored objects", Opt. Exp., 25(10), 11652-11672, (2017). This work was selected as **Editor's Pick**.
2. C. Mares, B. Barrientos, and A. Blanco, "Measurement of transient deformation by color encoding", Opt. Exp., 19(25), 25712-25722 (2011).
3. A. Blanco, B. Barrientos, and C. Mares, "Performance comparison of background-oriented schlieren and fringe deflection in temperature measurement, part 2: experimental evaluation", Opt. Eng., 55(6), 064104 (2016).
4. A. Blanco, B. Barrientos, and C. Mares, "Performance comparison of background-oriented schlieren and fringe deflection in temperature measurement: part I. Numerical evaluation", Opt. Eng., 55(5), 054102 (2016).

6.4.2 Congress works (18)

1. D. Blanco, B. Barrientos, A. J. Moore, and C. Mares, "Temperature Measurement of a Synthetic Jet Produced by a Helmholtz Cavity," in: Martínez-García A., Furlong C., Barrientos B., Pryputniewicz R. (eds) Emerging Challenges for Experimental Mechanics in Energy and Environmental Applications, Proceedings of the 5th International Symposium on Experimental Mechanics and 9th Symposium on Optics in Industry (ISEM-SOI), 2015. Pp. 145-151. Conference Proceedings of the Society for Experimental Mechanics Series. Springer, Cham (2017). DOI: 10.1007/978-3-319-28513-9_20.
2. D. Blanco, B. Barrientos, and C. Mares, "Comparison of BOS and fringe deflection in temperature measurement," ICO 2011, agosto de 2011, Puebla, Puebla, Méx. Proc. SPIE 8011, Ed. R. Rodriguez-Vera and R. Diaz-Uribe, 801180, pp. 11 (2011).
3. D. Migoni, B. Barrientos, C. Mares, "Out-of-plane deformation measurement of a pneumatic muscle by fringe projection and laser scanning," ISEM 2015, 17-21 de agosto, Gto. Gto. Méx. (2015).
4. M. Casas, C. Mares, B. Barrientos, D. Sarocchi, "Texture measurement of fine arts objects by optical techniques," Invited Talk, ISEM 2015, 17-21 de agosto, Gto. Gto. Méx. (2015).
5. C. Mares, B. Barrientos, D. Sarocchi, and M. Cerca, "Analysis of the dynamical behavior of dry granular avalanches by fringe projection and digital image correlation," ISEM 2015, 17-21 de agosto, Gto. Gto. Méx. (2015).
6. C. Mares, B. Barrientos, D. Sarocchi, M. Cerca, "Optimization of the color-coded technique for three-dimensional deformation," ISEM 2015, 17-21 de agosto, Gto. Gto. Méx. (2015).
7. M. C. Casas, B. Barrientos, D. Sarocchi, and C. Mares, "Reconstrucción del modelo 3D en alta resolución de la superficie de obras pictóricas por medio del método de proyección de franjas," IV Congreso latinoamericano de Arqueometría, 27 octubre, Méx., D. F. (2014).
8. C. Mares, B. Barrientos, M. Cerca, D. Sarocchi, and L. Serrano,"Fringes projection for 3D displacement analysis of experimental dry granular avalanches," GeoMod2014 Modelling in Geosciences, 31 agosto, Postdam, Ger. (2014).
9. B. Barrientos, C. Mares, D. Carreón, M. Cerca y R. Gutíerrez, "Medición simultanea de desplazamientos 3D y rotación," RUAG 2013, Geos, 33(1), p. 290, 06 de noviembre, Pto. Vallarta, Jal. Méx. (2013)..
10. G. Gutíerrez, C. Alcantara, D. Carreón, B. Barrientos y C. Mares, "Monitoreo de la deformación superficial en el sector Noreste del Peñòn del Marqués, Delegación Iztapalapa," RUAG 2013, Geos, 33(1), p. 290, 06 de noviembre Pto. Vallarta, Jal. Méx. (2013).
11. B. Barrientos, C. Mares y M. Cerca, "Medición de desplazamiento 3D de campo completo," RUAG 2013, Geos, 33(1), p. 292-293, 06 de noviembre, Pto. Vallarta, Jal. Méx. (2013).
12. R. Gutíerrez, C. Alcántara, D. Carreón, B. Barrientos y C. Mares, "Resultados de medición de la deformación del subsuelo mediante una estación de monitoreo mecánica en la Colonia Jacarandas de la Delegación Iztapalapa," RUAG 2013, Geos, 33(1), p. 291, 06 de noviembre, Pto. Vallarta, Jal. Méx. (2013).
13. A. Blanco, B. Barrientos, y C. Mares, "Medición de temperatura en el tambor de una secadora de ropa mediante deflexión de franjas," XXVI Reunión anual de Óptica, 17 de octubre, Hermosillo, Son. (2013).
14. C. Mares, B. Barrientos, M. Cerca, "Instantaneous full-field 3D displacements measurement," Advances in quantitative modeling Workshop 1, Sep 23-26, Postdam, Germany. (2013).
15. B. Barrientos, C. Mares, D. Carreon, M. Cerca, R. Gutíerrez, "Simultaneous measurement of 3D displacement and rotation of an active faulting," Advances in quantitative modeling Workshop 1, Sep 23-26, Postdam, Germany (2013).
16. D. Carreón, B. Barrientos, R. Gutíerrez, C. Mares and M. Cerca, "Instrumentation system for in situ monitoring of ground deformation in Iztapalapa, Mexico City," 108th Annual Meeting, Cordilleran Section of the Geological Society of America, marzo 29-31, Qro., Méx. (2012).
17. A. Blanco, B. Barrientos, C. Mares, "Análisis simultáneo de la sensitividad y precisión de las técnicas de deflexión de franjas y schlieren de fondo orientado para la medición de temperatura haciendo uso de codificación a color," Reunión Anual de Óptica XXV, octubre 08, Morelia, Mich. (2012).
18. C. Mares, B. Barrientos, and A. Blanco, "Measurement of transient deformation by color encoding," ICO 2011, agosto, Puebla, Puebla, Méx. (2011).

6.4.3 Citations to published works (13)

1. C. Mares, B. Barrientos and A. Blanco, "Measurement of transient deformation by color encoding", Opt. Exp., 19(25), 25712-25722 (2011).

1) L. F. Sese, E. A. Patterson, and F. A. Diaz-Garrido, "Moda shape measurement of large industrial components fringe projection with 2D-DIC," 24th International Congress on Sound and Vibration, London, July 23-27, ICSV 24 (2017).
2) Siegmann, Philip, Luis Felipe-Sese, and Francisco Diaz-Garrido. "Improved 3D displacement measurements method and calibration of a combined fringe projection and 2D-DIC system." *Optics and Lasers in Engineering* 88, 255-264 (2017).
3) López-Alba, E., et al. "Optical low-cost and portable arrangement for full field 3D displacement measurement using a single camera." *Measurement Science and Technology* 27.11, 115901 (2016).
4) W. L. Gubbels and G. S. Schajer, "Development of 3-D digital image correlation using a single color-camera and diffractive speckle projection," Exper. Mech., **56**(8), 1327-1337 (2016).
5) L. Sesé, E. Lopez-Alba, P. Siegmann, and F. A. Diaz, "Integration of fringe projection and two-dimensional digital image correlation for three-dimensional displacements measurements," Optical Engineering. 55. 121711. 10.1117/1.OE.55.12.121711 (2016).
6) Gubbels W. And Schajer G., "Three-dimensional digital image correlation using a single color-camera", in Advancement of optical methods in experimental mechanics, Vol. 3, Conf. Proc. SEM series, Ed. H. Jin, C. Schiammarella, S. Yoshhida and L. Lamberti, 315-324 (2015).
7) L. A. F. Sese, "Integración de proyecci[on de franjas y correlación digital de imágenes 2D para la medida de deformaciones y desplazamientos 3D," Tesis de Docotorado, Universidad de Jaen, (2014).
8) L. Felipe-Sesé, P. Siegmann, F. Díaz, and E. Patterson, "Integrating fringe projection and digital image correlation for high-quality measurements of shape changes", Opt. Eng., 53, 4, 044106 (2014).
9) L. Felipe-Sesé, P. Siegmann, F. Díaz, and E. Patterson, "Simultaneous in-and-out-of-plane displacement measurements using fringe projection and digital image correlation", Opt. Lasers Eng., 52, 66-74 (2014).
10) Z. Sun and Y. Zhou, "Assesing cardiac dynamics based on X-ray coronary angiograms," J. Multimedia, 8(1) 48-55 (2013).
11) L. Sesé, F. Díaz-Garrido, R. Vicente and P. Siegmann, "Comparativa de técnicas de filtrado de imágenes para el procesado conjunto de las técnicas de correlación digital de imágenes 2D y proyección de franjas," XIX Congreso Nacional de Ingeniería Mecánica, 8 pp., Esp. (2012).
12) L. Sesé, F. Díaz-Garrido, R. Vicente and P. Siegmann, "Calibración del montaje óptico para determinación de desplazamientos en el espacio mediante correlación digital de imágenes 2D y proyección de franjas," XIX Congreso Nacional de Ingeniería Mecánica, 7 pp., Esp. (2012).

2. D. Blanco, B. Barrientos, and C. Mares, "Comparison of BOS and fringe deflection in temperature measurement", ICO 2011, agosto de 2011, Puebla, Puebla, Méx. Proc. SPIE 8011, Ed. R. Rodriguez-Vera and R. Diaz-Uribe, 801180, pp. 11 (2011).

1) B. Zhang,, Z. G. Liu, and M. M. Zhao, "Three-dimensional dynamic visualization of premixed flame based on optical deflection tomography," J. Optoelectronics Laser, 26(10), 1947-1952, (2015).

6.4.4 Projects with industry (5)

1. B. Barrientos, C. Mares, R. Valdivia, "Diseño y desarrollo de un paquete de software para el cálculo de temperatura mediante imágenes schlieren", no. interno 1143.0609, CIATEQ, Qro., Qro. (10/08/2015-28/02/2016).
2. B. Barrientos, C. Mares, R. Valdivia y G. Garnica, "Diseño y aplicación de un sistema de velocimetría 2D dedicado a la visualización de flujo en una estufa", INNOVATEC 2012 CONACyT Proy. 181487, no. interno 1143.05.42 (firma convenio agosto 27 2012, fecha alta, oct 02), Empresa mabe, Qro., Qro. (07/09/2012-13/01/2014).
3. B. Barrientos, C. Mares, R. Valdivia y G. Garnica, "Análisis del flujo de aire en un secador industrial para la optimización del proceso de secado", CONCyTEG Fondos Mixtos 2012 Proy. 187415, no. interno 1143.05.40 (fecha alta, noviembre 01), Empresa Kodiak, León, Gto. (07/09/2012-07/07/2014).
4. B. Barrientos, C. Mares, R. Valdivia y G. Garnica, "Desarrollo de sistema óptico para el análisis experimental de fenómenos de dinámica de fluidos a través de la técnica de velocimetría por imágenes de partículas con enfoque a la optimización de consumo energético de secadoras de ropa domésticas", INNOVATEC 2012 CONACyT Proy. 178263, no. interno 1143.05.41 (firma convenio agosto 27 2012, fecha alta, oct 02), Empresa mabe, Qro., Qro. (07/09/2012-09/12/2013).
5. B. Barrientos, C. Mares, G. Garnica y R. Valdivia, "Diseño y construcción de sistemas de monitoreo de desplazamiento en la superficie del territorio de la Delegación Iztapalapa", Gobierno de la Delegación Iztapalapa, D. F. (22/04/2011-14/10/2012).